University of Texas at Tyler
Scholar Works at UT Tyler

Electrical Engineering Theses | Electrical Engineering

Spring 5-8-2012

Four-Coil Wireless Power Transfer Using Resonant Inductive Coupling

Sravan Annam

Follow this and additional works at: https://scholarworks.uttyler.edu/ee_grad

Part of the Electrical and Computer Engineering Commons

Recommended Citation

Annam, Sravan, "Four-Coil Wireless Power Transfer Using Resonant Inductive Coupling" (2012). *Electrical Engineering Theses.* Paper 19.
http://hdl.handle.net/10950/87

This Thesis is brought to you for free and open access by the Electrical Engineering at Scholar Works at UT Tyler. It has been accepted for inclusion in Electrical Engineering Theses by an authorized administrator of Scholar Works at UT Tyler. For more information, please contact tgullings@uttyler.edu.

APPLE 2023
Masimo v. Apple
IPR2023-00634

FOUR-COIL WIRELESS POWER TRANSFER USING RESONANT INDUCTIVE COUPLING

by

SRAVAN GOUD ANNAM

A thesis submitted in partial fulfillment
of the requirements for the degree of
Master of Science in Electrical Engineering
Department of Electrical Engineering

David M. Beams, Ph.D, PE, Committee Chair

College of Engineering and Computer Science

The University of Texas at Tyler
May 2012

The University of Texas at Tyler
Tyler, Texas

This is to certify that the Master's thesis of

SRAVAN GOUD ANNAM

has been approved for the thesis requirements on
April 4th, 2012

for the Master of Science in Electrical Engineering

Approvals:

Thesis Chair: David M. Beams, Ph.D., P.E.

Member: Hassan El-Kishky, Ph.D., P.E.

Member: Hector A. Ochoa, Ph.D.

Chair and Graduate Coordinator: Mukul V. Shirvaikar, Ph.D.

James K. Nelson, Jr., Ph.D., P.E.,
Dean, College of Engineering and Computer Science

Acknowledgements

I appreciate my advisor Dr. David M. Beams for his continuous teaching, guidance, support and patience throughout my thesis work. His vast knowledge and valuable suggestions were very helpful in achieving my target.

I thank my committee members Dr. Hassan El-Kishky and Dr. Hector A. Ochoa for their valuable time and reviews. I thank Dr. Mukul Shirvaikar for his continuous support from the beginning of my master's course. I am grateful to each and every professor and friends for their teachings and guidance.

I thank my family members for their love and encouragement. Finally I thank the almighty god for this wonderful life.

Table of Contents

List of Figure……...iii

List of Tables……...vi

Abstract……...vii

Chapter One: Introduction……1

1.1 Organization of thesis……2

Chapter Two: Background…….……...3

2.1 Early developments in wireless power transfer……...3

2.2 Methods for wireless power transfer.....5

2.3 Developments in wireless power transfer (WPT): 6

2.4 Review of prior research in WPT:.....8

Chapter Three: Development and experimental validation of a coupled-resonant model for wireless power transfer……..…… 11

3.1 Model development……...11

3.2 Matlab ® simulation program for analysis of four-coil WPT networks..……..13

3.3 Experimental validation of the four-coil WPT matlab model…...……..15

3.3.1 Experimental setup……17

3.3.2 Validation with D_{23} = 25.4mm……...……..18

3.3.3 Experimental results with D_{23} =38.1mm…….22

3.3.4 Experimental results with D_{23} = 50.8mm….……...24

3.4 Summary……...26

Chapter Four : Calculation of mutual inductance from magnetic vector potential for WPT applications……27

4.1 Calculation of mutual inductance from the magnetic vector potential……...28

4.2 Numerical methods for calculation of mutual inductance from the magnetic vector potential……30

4.3 Computation of self-inductance with the method of magnetic vector potential…...31

4.4 Empirical tests of numerical computation of self and mutual inductances……..32

4.4.1 Experimental coil descriptions and comparison of measured and calculated self-inductances……...…….33

4.4.2 Measured and calculated mutual inductances between a pair of coils……34

4.5 Application to inductors backed by ferrite……..……...37

4.5.1 Experiment in simulating inductance of a coil in proximity to two ferrite sheets 38

4.6 Summary…….....42

Chapter Five: Design of WPT systems by reflected impedances in loosely-coupled inductors……42

5.1 WPT system model: 42

5.2 Reflected impedance in mutually-coupled inductors with *RC* termination 44

5.3 Reflected impedance in mutually-coupled inductors with resistive termination: 49

5.4 Application of reflected impedances to the analysis of a four-coil WPT system: ...51

5.5 Application of reflected impedances to the design of a four-coil WPT system:.....54

5.6 Validation of the design methodology using impedance transformation.....58

5.6.1 Experimental method of design validation ..... ……..59

5.6.2 Summary of experimental results..... …….61

5.6.3 Discussion..... ……..64

5.7 Summary.....66

Chapter Six: Conclusions and future work……...……69

6.1 Conclusions 67

6.2 Future work 67

References……...……..68

List of Figures

Figure 2.1: Tesla's wireless energy apparatus as depicted in US patent 645,576……...3

Figure 2.2: Tesla's Wardenclyffe Tower……..…….4

Figure 2.3: Launch port (inductive charger for iPad2).....6

Figure 2.4: Samsung wireless charging hub for 3D glasses……7

Figure 3.1: Overall schematic of the four-coil wireless power transfer (WPT) system ……...11

Figure 3.2: Graphical user interface for WPT Model……....14

Figure 3.3: Definition of initial radius and horizontal pitch of a single-layer spiral coil …….16

Figure 3.4: Coil geometry of model-validation experiments…….17

Figure 3.5: Experimental apparatus for tests to validate Matlab WPT simulation program……..18

Figure 3.6: Simulated and measured input current I_1 vs. frequency.……20

Figure 3.7: Simulated and measured voltage across L_2 vs. frequency….……..20

Figure3.8: Voltage across L_3 vs. frequency…….....…21

Figure 3.9: Voltage across R_L vs. frequency …….……21

Figure 3.10: Simulated and measured input current I_1 vs. frequency……...…….22

Figure 3.11: Voltage across L_2 vs. frequency ……...23

Figure 3.12: Voltage across L_3 vs. frequency……...…23

Figure 3.13: Voltage across R_L vs. frequency……...…….24

Figure 3.14: Simulated and measured input current I_1 vs. frequency……....24

Figure 3.15: Voltage across L_2 vs. frequency …….……..25

Figure 3.16: Voltage across L_3 vs. frequency …….…….…….25

Figure 3.17: Voltage across R_L vs. frequency……...…….26

Figure 4.1: Basic four-coil WPT system……27

Figure 4.2: Geometry for computation of flux linkages and mutual inductance between closed paths L_1 and L_2……...…28

Figure 4.3: Geometry for computation of magnetic vector potential and mutual inductance…...29

Figure 4.4: Geometry for numerical estimation of magnetic vector potential and mutual

inductance……..30
Figure 4.5: Example of interleaved inductors for applying the magnetic-vector potential method to calculation of self-inductance of a spiral coil……32
Figure 4.6: GUI of the solenoid creator…….33
Figure 4.7: GUI of Matlab mutual inductance calculator 36
Figure 4.8: Inductors L_A and L_B positioned above a sheet of high-permeability ferrite material……37
Figure 4.9: Solenoid coils mounted coaxially ……..……38
Figure 4.10: Simulated and measured results for mutual inductance between two solenoid coils vs. height over a ferrite sheet……...…..38
Figure 4.11: Geometry for experiments for determining the inductance of a spiral-wound coil between ferrite sheets……...……..40
Figure 4.12: Measured and simulated inductance of a spiral-wound coil between ferrite sheets……..41
Figure 5.1: Coupled-inductor model for resonant wireless power-transfer system……. 43
Figure 5.2: Coupled inductors with RC termination with voltage source excitation……46
Figure 5.3: Equivalence of mutually-coupled inductors with RC termination and a single coil with reflected resistance R_{ref} and reactance X_{ref} ……...……47
Figure 5.4: Resistive and reactive components of the input impedance at the terminals of L_a for values specified and for k_{ab} = 0.2 ……..……48
Figure 5.5: Resistive and reactive components of the input impedance at the terminals of L_a for values specified and for k_{ab} = 0.4 ……...……...……49
Figure 5.6: Resistive and reactive components of the input impedance at the terminals of L_a for values specified and for k_{ab} = 0.6……..…….…….……...49
Figure 5.7: Mutually-coupled inductors with resistive termination……..50
Figure 5.8: Proposed equivalent circuit reducing a four-coil WPT system to a single-loop circuit including reflected resistances and reactances.....52
Figure 5.9: Reflection of a capacitive reactance into L_1 due to mutual inductance M_{13} and inductor current i_3 ……...……...55
Figure 5.10: WPT design worksheet based on reflected impedances……57
Figure 5.11: Physical arrangement of single-layer spiral coils used in validation experiments…59
Figure 5.12: Experimental apparatus, showing physical arrangement of coils, resonating capacitors, and load resistance ……...…...60
Figure 5.13: Measured resistance and effective inductance of L_3 (including resistance and

reactance reflected into L_3 from L_4) ……...…...61
Figure 5.14: Measured resistance and inductance looking into L_2 ……...61
Figure 5.15: Measured resistance and inductance looking into L_1……...61
Figure 5.16: Connection of the WPT network to a sinusoidal signal source…….62
Figure 5.17: Network including M_{24} …….……...….66

List of Tables

Table 3.1: Parameters of coils used in WPT model validation……..16

Table 4.1: Physical description of solenoid coils……..……...34

Table 4.2: Measured vs. computed mutual inductance…….……..….36

Table 4.3: Spiral coil description used in presence of two ferrite sheets……..……...39

Table 5.1: Fixed self- and mutual inductances in design-validation experiments 62

Table5.2:Variable mutual inductances vs. source-to-load spacing D_{23} …….……..63

Table 5.3:Reflected resistance and reactance from coil 4 into coil 3,and inductance and resistance measured at the terminals of L_3 for the network of Figure 5.13…..…….63

Table 5.4: Reflected resistance from coil 3 into coil 2, total resistance at the terminals of L_2 (R_{eff2}), and measured inductance of L_2 (L_{eff2}) vs source-to-load spacing D_{23} for a network similar to that of Figure 5.14……...…….64

Table 5.5: Reflected resistance from coil 2 into coil 1, total resistance at the terminals of L_1 (R_{eff1}) and measured inductance of L_1 (L_{eff1}) vs source-to-load spacing D_{23} for a network similar to that of Figure 5.15……...…….64

Table 5.6: Input voltage V_S and magnitude and phase of input current I_1 vs. source-to-load spacing D_{23}…….……...65

Table 5.7: Efficiency of power transfer of the WPT network……....65

Abstract

Four-Coil Wireless Power Transfer using Resonant Inductive Coupling

Sravan Goud Annam

Thesis Chair: David M. Beams, Ph. D, PE.

The University of Texas at Tyler

May 2012

With the developments of mobile and implantable devices, wireless power transfer (WPT) has become increasingly attractive to free a variety of electronic systems from power cords and batteries. Resonant inductive coupling is the leading technology of WPT, offering high efficiencies (>75%) with power levels from microwatts to hundreds of watts.

This thesis focuses on a resonant four-coil inductive WPT technology. It develops numerical models of the four-coil WPT system (incorporated into a Matlab simulator) and validates them by experiment. It then develops numerical tools using Matlab for computing self- and mutual inductances for inductors of arbitrary shape and orientations using the method of magnetic vector potential and validates these tools by experiment. Inductance-calculation tools are designed to be user-friendly and are intended to be employed as a substitute for FEA (Finite Element Analysis).

Effects of high magnetic permeability materials like ferrite sheets on the self- and mutual inductance of coils are studied, and Matlab-based numerical tools are developed to analyze such effects. These tools were validated by experimental work.

A proposed design methodology employing the method of reflected impedances in loosely-coupled inductors is applied to the design of a four-coil WPT presented in this

thesis. This method reflects impedances sequentially through the inductors from the system load to the driving source and is incorporated in a spreadsheet calculator. A design derived from this method is subjected to experimental validation and efficiencies exceeding 76% are noted with various spacings between the transmitting and receiving coil pairs. The method is shown to be useful for "first-pass" design, but significant effects are noted due to mutual inductances neglected in the design procedure. The full model is necessary for accurate simulation results. Conclusions and suggestions for future work are presented.

Chapter One
Introduction

Recent developments have shown a revival of interest in the possibility of transferring significant amounts of electric power over short distances (up to tens of centimeters) through wireless power transfer (WPT). The idea of WPT has taken various forms since its inception in the late 19thcentury. WPT is being considered for replacement of wires and batteries in various applications; for example, WPT can be used to recharge laptop computers by means of wireless power hotspots built into desks and tables. Such wireless power hotspots may even eliminate the use of external battery chargers. WPT is moving from a research and development stage into a demonstration stage and slowly into application.

Current methods of WPT can be grouped into near and far-field applications. Far-field applications consist of beams of electromagnetic radiation of various frequencies which include radio, microwave, and laser devices.

Near-field applications are currently implemented by inductive and resonant inductive transfer, which use the non -radiative portion of the electromagnetic field. A near-field WPT system resembles an air-core transformer with the primary winding separated from the secondary by an air gap. The power transfer capability and efficiency of inductive coupling decrease with distance between the windings. With the effect of resonant inductive coupling, the loss of efficiency can be overcome to some extent. But efficient resonant induction is highly dependent on coil quality factor Q which increases for frequencies below the coil self-resonance. Hence, resonant inductive coupling systems usually operate in the frequency range of 10 kHz to 10 MHz.

Resonant inductive coupling has been applied to contactless battery charging systems in consumer electronics [1], powering desktop peripherals [2], charging of electric-vehicle batteries [3], and powering of endoscopic robots [4].

The goal of this thesis is in the analysis and design of WPT systems using resonant inductive coupling. Multiple MATLAB ®based tools and analysis methods will be developed.

In practice the application of such system involves coils of various geometries and variable orientations. Such variable geometries are often investigated through finite-element analysis (FEA), e.g., [5]. However, a simple tool for computing mutual inductances between such coils that did not require expertise in FEA or access to FEA software could have significant benefit to the designer of WPT systems.

The four-coil wireless-power transfer (WPT) system has been shown to transfer electric power over short distances with high efficiency by means of loosely-coupled inductors and resonating capacitors. However, there are many degrees of freedom and many variables to manipulate, and the complexity of the design space makes *a* prior design difficult. This thesis work attempts to reduce that complexity by identifying the most-important parameters and to provide a theoretical basis for experimental observations.

1.1 Organization of thesis

This thesis is divided into six chapters. Chapter Two discusses the early developments, applications and prior research on WPT. Chapter Three describes the analytical expressions and numerical models of a four-coil WPT system. Chapter Four describes analytical expressions and computational methods used to determine mutual inductance between coils of arbitrary size and physical orientation. Chapter Five develops a method based upon reflected impedances of design of a four-coil WPT system. Chapters Three to Five include experimental validation of the numerical models. Chapter Six discusses conclusions and directions for future work.

Chapter Two
Background

2.1 Early developments in wireless power transfer

The concept of wireless power transfer (WPT) began with the experiments of Nikola Tesla at the end of the 19th and beginning of the 20th centuries. Tesla proposed a concept of electrodynamic induction using a Tesla coil-like device to create an alternating electric field with extremely high strength that could provide energy to a receiver. Tesla thought this energy distribution method would be used in interior applications, e.g., allowing lighting fixtures to be moved anywhere within a room without need for wires. Figure 2.1 is an illustration of the WPT system proposed by Tesla.

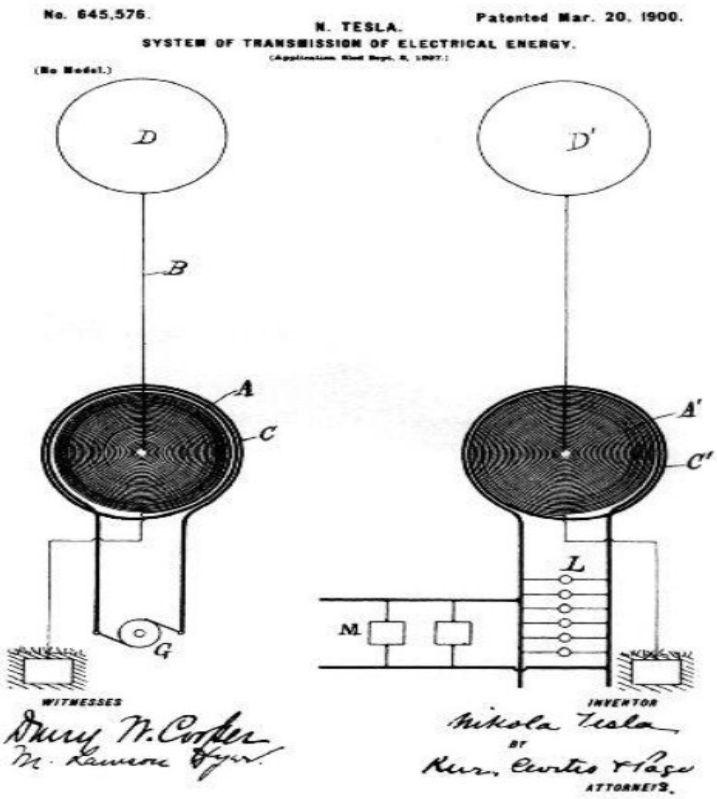

Figure 2.1: Tesla's wireless energy apparatus as depicted in US patent 645,576 [6]

Figure 2.1 consists of transmitting and receiving apparatus. The transmitting apparatus includes coils A and C (wound as large-diameter spiral coils), terminal electrode D, and generator G. Coil A is the primary side of a transformer whose secondary winding is coil C. One terminal of coil A is connected to terminal D by conductor B, while the other end is connected to earth ground. At the receiving side a transformer of similar construction is employed with coil A' as the primary and C' as the secondary. The elevated terminal D' is connected to the center of coil A' via conductor B'; the other terminal of coil A' is connected to ground. The terminals of C' are connected to lamps L and motors M.

Tesla's findings led him to design the Wardenclyffe plant [7] as a wireless power transmitter where the Wardenclyffe tower was used to serve as a wireless power transmission facility. At Wardenclyffe, he operated across a range of frequencies from 1 kHz to 100 kHz at powers up to 1.5 MW. Tesla thought excitation at these frequencies would yield the most economical method of power transmission, and his apparatus indicated an efficient range between 30 – 35 kHz.

Despite the novelty of Tesla's demonstration and his personal efforts to commercialize wireless power transmission, he had to put a halt to his experiments due to lack of funds.

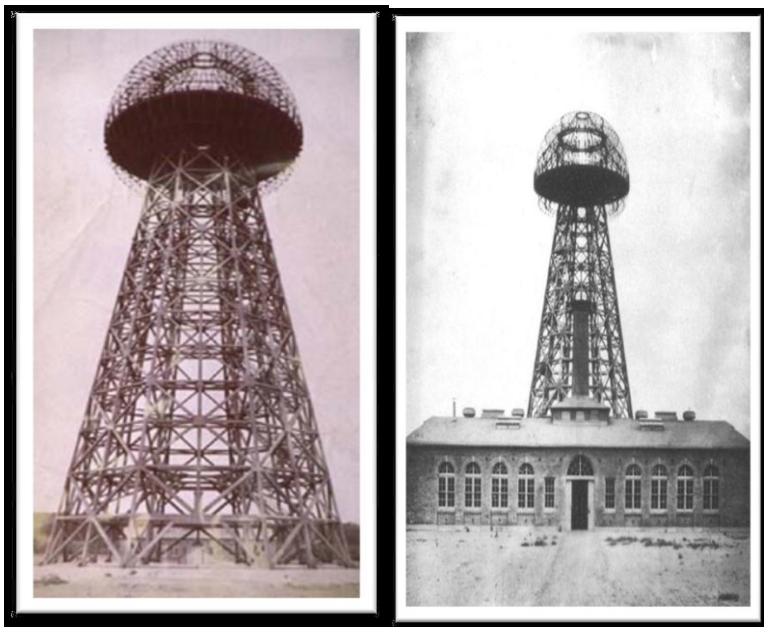

Figure 2.2: Tesla's Wardenclyffe Tower

Since Tesla's work, researchers have sought more efficient methods for WPT.A complete mathematical understanding of the coupled circuits used to build the transmitter and the receiver was first published by Frederick Terman in 1935 [8]. The idea of using microwave power transmission was proposed by William C. Brown in 1961 [9].

In 2007, a group of researchers at the Massachusetts Institute of Technology (MIT) revisited Nikola Tesla's original idea of transporting energy over a distance without a carrier medium using electromagnetism. A demonstrator system was constructed using self-resonant coils, and achieved a transfer power of 60 W with 40% efficiency over distances in excess of 2 m.

2.2 Methods for wireless power transfer

Methods for conducting wireless power transfer are classified as follows

Radio Waves: Power transmission by radio waves dates back to the early work of Heinrich Hertz. The advantage of using radio waves for wireless power transfer is that high-power radio technology is fairly mature.

Inductive: Inductive power transfer systems are defined as systems where energy is transferred from a primary winding to a secondary winding using an alternating magnetic field. The advantage of inductive WPT is that it is a low-cost and highly-efficient method of transferring power. The design of an induction link is fairly straightforward and surprisingly efficient at short distances. The main drawback of using this method is the limitations in coil geometries and distance.

Lasers: The main problems with laser power transfer are the low efficiencies and safety concerns. Lasers operating at 1.4μm have shown efficiencies up to 30% when converted into electrical energy through photonic detectors.

Ultrasound: In addition to laser wireless power transfer, a new concept for wireless power transmission that employs ultrasonic air transducers has been developed. In ultrasonic wireless power transmission, a transmitter composed of a pulse generator, an amplifier, and a horn radiator, transfers power through the air. A receiver composed of a receiving transducer, a rectifier, and a capacitor, receives the power and applies it to a load. These systems have promise, but have not been demonstrated over large distances.

With time, ultrasonic wireless power transfer may become more promising in low-power applications.

2.3 Developments in wireless power transfer (WPT):

WPT technology can be applied in different fields and environments. The ability to transfer power safely, efficiently, and over a distance can improve products by making them more convenient and reliable.

Products employing WPT are classified based on their usage method as either direct or automatic supply. Direct use means supplying power directly from the source to the load, while automatic supply means recharging batteries of battery operated devices whether they are in use or not. There are several applications [10] for wireless transfer of power in which the following main areas can be mentioned.

Systems for wireless charging of batteries in mobile electronics (e.g., cellular telephones, laptop computers, game controllers) have been designed. In such devices wireless charging can be done even when the devices are in use. For example, iPort (San Clemente CA) has launched an inductive charger for the iPad2 called "Launch Port" [11] shown in Figure 2.3. The wireless charging system of this product starts charging an iPad wirelessly as soon as the Power Shuttle is docked onto the wall station or base station. The power Shuttle (receiving part) is the hard case, the base station is a tabletop-mounted charging location, and the wall station is a wall-mounted charging location for the Power Shuttle.

Figure 2.3: Launch port (inductive charger for iPad2)

Biomedical devices such as pacemakers and electric nerve stimulator devices have used inductive charging for many years. Since the devices are located inside the body, it is very attractive to charge their batteries wirelessly. A physical contact that penetrates the skin would be uncomfortable and could lead to infections. The gap between transmitter and receiver in this kind of application is normally 1–2 cm. Heat generations inside the body must be limited, and the implanted devices must remain at approximately body temperature during charging. Therefore, power transfer is normally under 50 W.

High reliability and low maintenance costs are important in aerospace, military, and industrial applications. Such applications frequently use contactless power transfer through rotary transformers. For example, rotating radar heads avoid the use of slip rings by means of contactless power transfer. Contactless power transfer using rotary transformers permits free-moving capability in systems such as robot arms.

Corporations such as Panasonic, Philips and Texas Instruments are using contactless power transfer for recharging batteries of small electric appliances (e.g., electric toothbrushes, wireless computer mice, and remote controls).

Samsung's "Wireless Charging Hub" [12] eliminates the need of wires for charging electronic 3D glasses. Up to four pairs of 3D Glasses can be charged by placing them around the rim. Figure 2.4 shows a pair of 3D glasses being recharged by a wireless charging hub.

Figure 2.4: Samsung wireless charging hub for 3D glasses

2.4 Review of prior research in WPT:

A brief literature survey reveals various techniques and different applications of WPT, a number of previous published papers on conducting WPT ([13]-[25]) uses either the method of inductive coupling or resonant inductive coupling.

Cannon [13] describes a WPT system using resonant inductive coupling at 8.3 MHz, with the output power being delivered to multiple small loads (LEDs) with an output power of 28.2 mW at an efficiency of 40%-50% of input power.

Shen et al [14] have described circuit analysis of WPT by coupled magnetic resonance. The resonating frequency of coils was 9.4 MHz and maximal efficiency was obtained by placing the two coaxially-aligned coils 3cm apart.

Low [15] describes the design and test of a loosely-coupled planar WPT System that uses a class E transmitter operating at a frequency of 134 kHz, delivering an output power of 295W at 75.7% efficiency.

Choi and Seo [16] describe a magnetic resonance-based WPT system which uses a meta-material which has a relative permeability of –1. They report an efficiency of energy transfer efficiency of about 80% over a distance of 1.5m at a frequency of 23.2 MHz using the meta-materials. Without the negative-permeability material, the reported efficiency dropped to 60%. Meta-materials are artificial composites in which the electromagnetic properties can be engineered to achieve properties (e.g., negative permeability) not observed in pure materials.

Karalis [17] describes an efficient wireless non-radiating mid-range energy transfer method and discusses macroscopic applications such as the delivery of power to robots and/or computers in a factory room. In the microscopic world, where much smaller wavelengths would be used and smaller powers are needed, one could use it to implement optical interconnects for CMOS electronics, or to transfer energy to autonomous nano-objects (e.g. MEMS or nano-robots).

Si [18] describes a new method called ZVS (Zero voltage Switching) used for stabilizing the operating frequency of a resonant converter for wireless power transfer to implantable biomedical sensors.

Beh, Imura, Kato and Hori [19] have demonstrated a method for improving the efficiency of resonant magnetic coupling using an impedance-matching technique. An

application was developed for charging electric vehicle (EV) batteries. The operating frequency of the source is 13.56MHz and the reported efficiency is approximately 90% at 1m distance with 60W output power.

Chen [20] explored a conceptual WPT system that introduces a tuning method to transfer a predetermined amount of power using loosely-coupled coils at an efficiency of 73% while delivering an output power of 150W with an operating frequency of 10MHz. A team of researchers from Massachusetts Institute of Technology led by Kurs [21], presented a quantitative model describing the power transfer over a distance somewhat greater than 2m at an efficiency up to 40% while delivering 60W. This system used spiral-wound coils and had an operating frequency of 5.9 MHz.

Su and Liu [22], introduced a new method based on a formula used for calculating mutual inductance of movable planar coils on parallel surfaces. Using this formula, a new and useful tool for calculating mutual inductance between a movable planar coil and a fixed surface was made available. They proposed that this technique could be used in a wireless battery charging platform.

Low, Casanova and Lin [23], have demonstrated a design method using series- and parallel-impedance transformation in a system of loosely-coupled planar coils capable of supporting multiple receivers. This paper states that an increase in power can be achieved by increasing the supply voltage and by increasing the coupling between the coils. Efficiency greater than 55% was reported at an operating frequency of 240 kHz.

Xin , Yan, and Wang [24] introduced an application of WPT operating at 400kHz to power an active capsule endoscope .Their system included a class D or E inverter, an external transmitting coil, and multiple secondary (receiving) coils placed within the body. This paper emphasizes the importance of winding coils with Litz wire to reduce losses due to skin effect and proximity effect.

Imura [25] described the charging of an electric car using resonant magnetic coupling. The system can provide a convenient charging system which can recharge EVs wirelessly and automatically when they are parked. In this paper, a contactless power transfer (CPT) system employing electromagnetic resonant coupling was described and its feasibility was studied, emphasizing antenna characteristics. Resonant magnetic coupling can transmit power wirelessly even if there is only a low degree of magnetic

coupling. High efficiency may be achieved even with significant air gaps. Efficiencies greater than 90% were reported for spacings less than 200mm between the transmitting and receiving antennas operating at their resonant frequencies. Since minimum ground clearance of passenger vehicles ranges typically from 90 mm to 200 mm, this system is particularly suitable for EV charging applications.

Chapter Three

Development and experimental validation of a coupled-resonant model for wireless power transfer

3.1 Model development

Resonant inductively-coupled WPT systems may employ two- or four-coil methods. The four-coil method is the focus of this thesis. A proposed model of a four-coil WPT system is shown in Figure 3.1. The WPT system consists of four coils- input coil L_1, transmitting coil L_2, receiving coil L_3, and load coil L_4. Three capacitors C_1 –C_3 and a load resistance R_L complete the system. The system is energized by an AC voltage source v_s which has an output resistance of R_s. Losses in each of the four loops are modeled by including equivalent series resistance (ESR) elements R_1–R_4. It is assumed that all four inductors are coupled through mutual inductances M_{12}, M_{13}, M_{14}, M_{23}, M_{24}, and M_{34}.

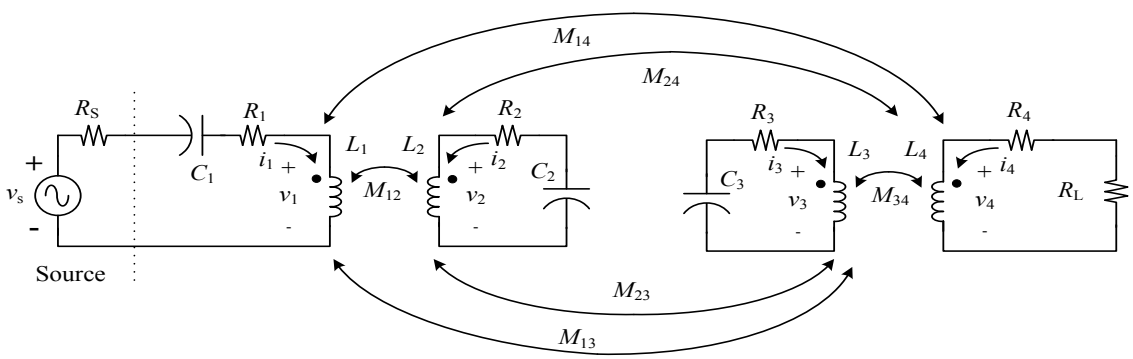

Figure 3.1: Overall schematic of the four-coil wireless power transfer (WPT) system. Components of the system are described below

The detailed nomenclature of Figure 3.1 is as follows:

v_s: Open-circuit voltage of an AC voltage source driving the WPT system.

R_S: Source resistance (Thévenin-equivalent resistance) of the ac voltage source.

L_1: Input-loop inductor.

C_1: Input-loop series capacitor.

R_1: Total equivalent series resistance (ESR) in the input loop consisting of the sum of the ESRs of L_1 and C_1.

L_2: Inductor of first (input-side) resonant *LCR* circuit.

C_2: Resonating capacitor of input-side resonant *LCR* circuit.

R_2: Total ESR in the input-side resonant *LCR* circuit, consisting of the sum of the individual ESRs of L_2 and C_2.

L_3: Inductor of second (output-side) resonant *LCR* circuit.

C_3: Resonating capacitor of output-side resonant *LCR* circuit.

R_3: Total ESR in the output-side resonant *LCR* circuit, consisting of the sum of the individual ESRs of L_3 and C_3.

L_4: Inductor of output loop.

R_4: ESR of L_4.

R_L: Load resistance.

M_{12}: Mutual inductance of L_1 and L_2.

M_{13}: Mutual inductance of L_1 and L_3.

M_{14}: Mutual inductance of L_1 and L_4.

M_{23}: Mutual inductance of L_2 and L_3.

M_{34}: Mutual inductance of L_3 and L_4.

Equations (3.1)–(3.8) describe the system of Fig. 1 under steady-state excitation by a sinusoidal voltage at angular frequency ω:

$$v_1 = j\omega L_1 i_1 + j\omega M_{12} i_2 + j\omega M_{13} i_3 + j\omega M_{14} i_4 \tag{3.1}$$

$$v_2 = j\omega M_{12} i_1 + j\omega L_2 i_2 + j\omega M_{23} i_3 + j\omega M_{24} i_4 \tag{3.2}$$

$$v_3 = j\omega M_{13} i_1 + j\omega M_{23} i_2 + j\omega L_3 i_3 + j\omega M_{34} i_4 \tag{3.3}$$

$$v_4 = j\omega M_{14} i_1 + j\omega M_{24} i_2 + j\omega M_{34} i_3 + j\omega L_4 i_4 \tag{3.4}$$

$$v_s = \left(R_1 + R_S \frac{1}{j\omega C_1} \right) i_1 + v_1 \tag{3.5}$$

$$v_2 = -\left(R_2 + \frac{1}{j\omega C_2} \right) i_2 \tag{3.6}$$

$$v_3 = -\left(R_3 + \frac{1}{j\omega C_3}\right) i_3 \tag{3.7}$$

$$v_4 = -(R_4 + R_L) i_4 \tag{3.8}$$

Eqs. (3.1)–(3.8) may be expressed compactly in matrix form as given in Eq. (3.9):

$$\begin{bmatrix} j\omega L_1 & j\omega M_{12} & j\omega M_{13} & j\omega M_{14} & -1 & 0 & 0 & 0 \\ j\omega M_{12} & j\omega L_2 & j\omega M_{23} & j\omega M_{24} & 0 & -1 & 0 & 0 \\ j\omega M_{13} & j\omega M_{23} & j\omega L_3 & j\omega M_{34} & 0 & 0 & -1 & 0 \\ j\omega M_{14} & j\omega M_{24} & j\omega M_{34} & j\omega L_4 & 0 & 0 & 0 & -1 \\ R_1 + R_S + \frac{1}{j\omega C_1} & 0 & 0 & 0 & 1 & 0 & 0 & 0 \\ 0 & R_2 + \frac{1}{j\omega C_2} & 0 & 0 & 0 & 1 & 0 & 0 \\ 0 & 0 & R_3 + \frac{1}{j\omega C_3} & 0 & 0 & 0 & 1 & 0 \\ 0 & 0 & 0 & R_4 + R_L & 0 & 0 & 0 & 1 \end{bmatrix} \times \begin{bmatrix} i_1 \\ i_2 \\ i_3 \\ i_4 \\ v_1 \\ v_2 \\ v_3 \\ v_4 \end{bmatrix} = \begin{bmatrix} 0 \\ 0 \\ 0 \\ 0 \\ v_s \\ 0 \\ 0 \\ 0 \end{bmatrix} \tag{3.9}$$

Solving Eq. (3.9) is relatively straightforward using Matlab ®. Solution with other tools (e.g., Excel) is also possible, although tools that do not support complex numbers will require independent solution of real and imaginary components of Eq. (3.9).

3.2 Matlab ® simulation program for analysis of four-coil WPT nnetworks

A Matlab-based simulator (wireless_power_transfer5) was designed for a four-coil WPT system utilizing matrix equation Eq. (3.9). Figure 3.2 below shows the graphical user interface (GUI) of this program.

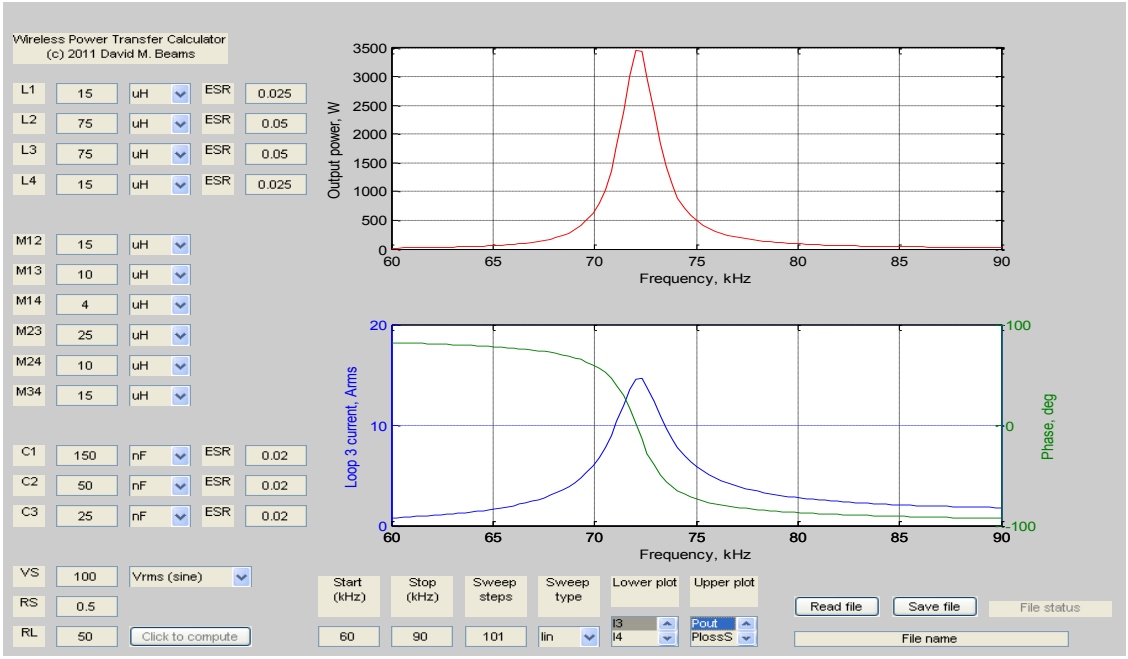

Figure 3.2: Graphical user interface for WPT model

The GUI of wireless_power_transfer5 allows users to enter the following network parameters:

- coil inductances L_1–L_4 (specified in mH, μH, or nH);
- mutual inductances M_{12}–M_{34} (specified in mH, μH, or nH, or as flux-coupling coefficients);
- capacitances C_1–C_3 (specified in μF, nF, or pF);
- ESRs of inductors and capacitors (Ω);
- load resistance R_L (Ω);
- Open-circuit generator voltage v_s;
- Output resistance of the generator R_S (Ω);
- Frequency sweep parameters (range, points, linear/logarithmic).

The user may select the type of input voltage value v_S (as a sine wave in peak, peak-to-peak, or *rms*, or as a square wave with the *rms* value of the fundamental component used for analysis).

Physically impossible values of mutual inductance or flux-coupling coefficients are flagged, and the computations are disabled in these circumstances. The following output variables may be observed.

- Loop currents I_1- I_4 magnitude (A_{rms}) and phase (degrees);
- Inductor voltages V_1-V_4, magnitude(V_{rms}) and phase (degrees);
- Total power (P_{in}) delivered by source v_s, W;
- Output power (P_{out}) delivered to load resistor R_L, W;
- Power loss (P_{losss}) in source resistance R_s, W;
- Power loss (P_{loss1}) in the total ESR of the input (L_1- C_1) loop, W;
- Power loss (P_{loss2}) in the total ESR of the first resonant (L_2- C_2) loop, W;
- Power loss (P_{loss3}) in the total ESR of the second resonant (L_3- C_3) loop, W;
- Power loss (P_{loss4}) in the ESR of L_4, W;
- Efficiency (P_{out}/P_{in}).

Voltages and currents vs. frequency are plotted with separate *y*-axes for magnitude and phase. Two independent variables may be simultaneously displayed, one in each of the two plot windows. The phase of the voltage source is taken as the reference (0°). The choice of the voltage source allows the user to specify voltages as sinusoidal (zero-to-peak, peak-to-peak, or *rms*) or square wave, in which only the fundamental component is presumed to play a part. (The excitation voltage is assumed to be the *rms* value of the fundamental component of the square wave).

3.3 Experimental validation of the four-coil WPT Matlab model

Experiments were performed to validate the four-coil WPT Matlab model and the simulation program *wireless_power_transfer5* by arranging four parallel, coaxial spiral coils. Coil self- and mutual inductances were measured and compared to the calculated values obtained from Matlab simulators that use the method of magnetic vector potential which is described in detail in Chapter Four.

Self-inductance of the coils were calculated using a Matlab simulator (named spiral_creator6.m) and measured at 100 kHz using the "L_s" measurement mode (resolving the inductor into a series connection of an inductance and a resistance) of an Agilent 4362 LCR Bridge. (This Matlab coil simulator is part of a series of simulators for creating models of spiral, solenoid, and rectangular coils). Table 3.1 gives the parameters of these coils.

Table 3.1: Parameters of coils used in WPT model validation

Coil	L_1	L_2	L_3	L_4
Turns	16	12	16	13
Horizontal pitch, mm	1.52	1.52	1.52	1.52
Initial inner radius, mm	33.52	43.18	34.55	35.56
Measured inductance, μH	33.3	19.4	32.2	22.4
Calculated inductance, μH	33.7	20.7	34.6	24.1
Coil file name	13sept16TAspiral	13sept12Tspiral	13sept16TBspiral	13sept13Tspiral

Figure 3.3 shows the geometry of a spiral coil initial radius and horizontal pitches are illustrated.

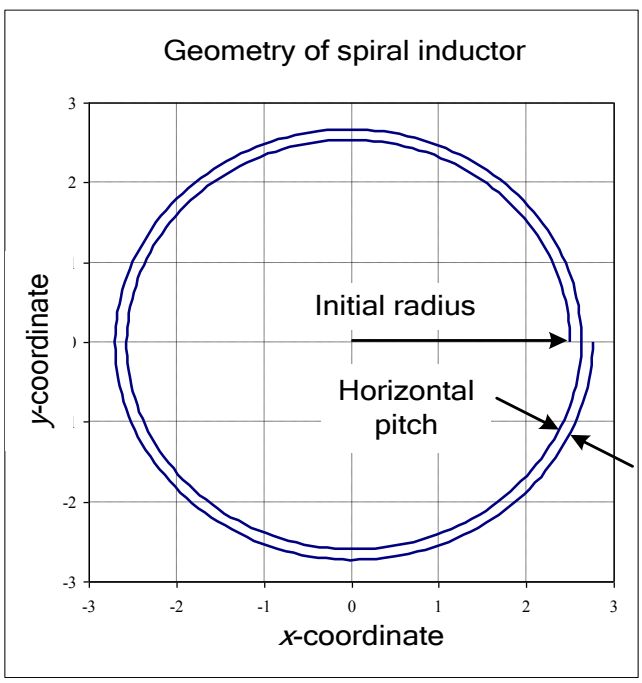

Figure 3.3: Definition of initial radius and horizontal pitch of a single-layer spiral coil

The geometry of the four inductors is illustrated in Figure 3.4. Three sets of experiments were performed, each with different spacing values of D_{23} (the spacing between L_2 and L_3). The distances between L_1–L_2 and L_3–L_4 were unchanged in all experiments.

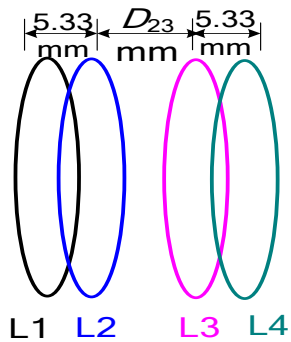

Figure 3.4: Coil geometry of model-validation experiments

Mutual inductance of the spiral coils were calculated using a Matlab simulator (mutual_inductance_calculator5.m) which computes the mutual inductance by means of the magnetic vector potential (described in Chapter Four). The mutual inductance of each pair of coils was measured by measuring their inductances in both series-aiding and series-opposing connection. The mutual inductance M was computed as $0.25\times(L_{S+}-L_{S-})$, where L_{S+} is the inductance of the coil pair in series-aiding connection, and L_{S-} is the inductance in series-opposing connection. All inductance measurements were performed at 100 kHz using the "L_s" measurement mode of an Agilent 4362 LCR Bridge.

3.3.1 Experimental setup

Tests began on 1 November 2011 to determine whether the model underlying the Matlab simulation of the WPT system (wireless_power_transfer5.m) is valid. The circuit in Figure 3.5 is the experimental setup. An HP33120 Arbitrary Waveform Generator is used as a signal source to drive a circuit consisting of an LT1220 operational amplifier and LT1010 buffer with an additional output resistance of 50Ω.

The voltage at the oscilloscope attachment point is assumed to be the open-circuit voltage of the voltage source driving the WPT system. This voltage was verified and regulated manually as necessary to maintain a fixed value of open-circuit source voltage for all experiments. This voltage also provided the phase reference for all other phase

measurements. The 50Ω resistance of the buffer circuit is taken as the output resistance R_S of the voltage source driving the WPT system.

Parasitic resistances R_1, R_2, R_3, and R_4 are the parasitic series resistances (ESRs) of L_1, L_2, L_3, and L_4, respectively; measurements of capacitors with the 4362 LCR Bridge showed their ESRs to be negligible compared to those of the coils. The capacitors' ESRs were thus assumed to be zero. The measured values of R_2–R_4 were entered into the Matlab simulation as the ESRs of their associated inductors. A 1Ω current-sense resistor was installed in series with the L_1-C_1 input network. The value for the ESR of L_1 entered into the Matlab simulation was the sum of ESR R_1 and the current-sense resistor.

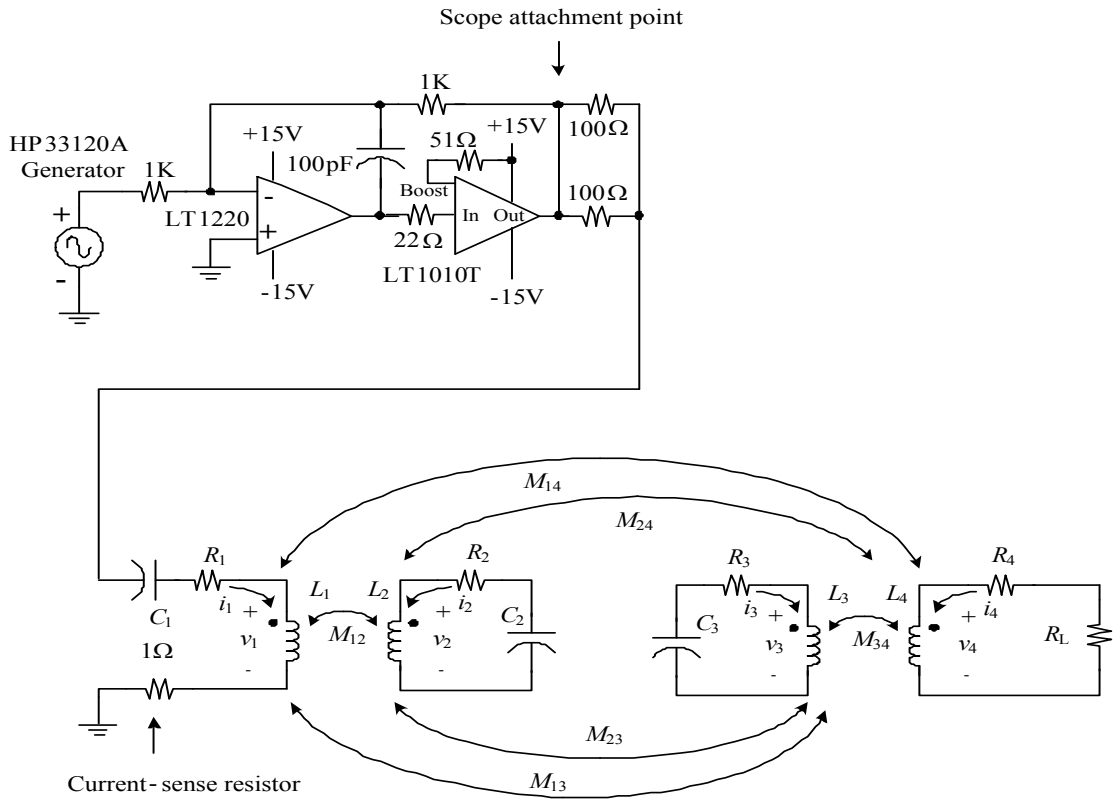

Figure 3.5: Experimental apparatus for tests to validate Matlab WPT simulation program

3.3.2 Validation with D23 = 25.4mm

Validation began by arranging all the four spiral coils as shown in the Figure 3.4 with coil center-to-center spacing between coils L_2- L_3 (D_{23}) equal to 25.4 mm.

Data were taken at frequencies from 75 kHz to 125 kHz in increments of 2 kHz. Parameters measured were input current I_1 (determined from the measured voltage across

the current-sense resistor), voltage V_{L2} across the terminals of coil L_2 , voltage V_{L3} across the terminals of L_3, and voltage V_{RL} across the load resistor R_L. The simulator program does not directly compute voltages across the inductor terminals; it computes the only the inductive components. Simulated values of V_{Lx}, the voltage at the terminals of inductor L_x, were calculated from simulated values of V_x, (the voltage due to inductive effects), R_x (ESR of inductor L_x), and I_x (current in inductor L_x) from the following relationships:

$$|V_{Lx}| = \sqrt{\left[|V_x|\cos(\phi_x)+|I_x|R_x\cos(\theta_x)\right]^2+\left[|V_x|\sin(\phi_x)+|I_x|R_x\sin(\theta_x)\right]^2} \qquad (3.10)$$

$$\angle V_{Lx} = \tan^{-1}\left[\frac{|V_x|\sin(\phi_x)+|I_x|R_x\sin(\theta_x)}{|V_x|\cos(\phi_x)+|I_x|R_x\cos(\theta_x)}\right] \qquad (3.11)$$

The parameters of Eqs. (3.10) and (3.11) are as follows:

$|V_{Lx}|$ is the magnitude of the voltage across the terminals of physical inductor L_x;

$\angle V_{Lx}$ is the phase angle of the voltage across physical inductor L_x;

$|V_x|$ is the magnitude of the voltage across the inductive component of inductor L_x;

$|I_x|$ is the magnitude of the current flowing in inductor L_x;

R_x is the ESR of inductor L_x;

ϕ_x is the phase angle of V_x;

θ_x is the phase angle if I_x.

Figure 3.6 compares simulated and measured input I_1 and phase of the current I_1 as a function of frequency for the test conditions in Figure 3.4.

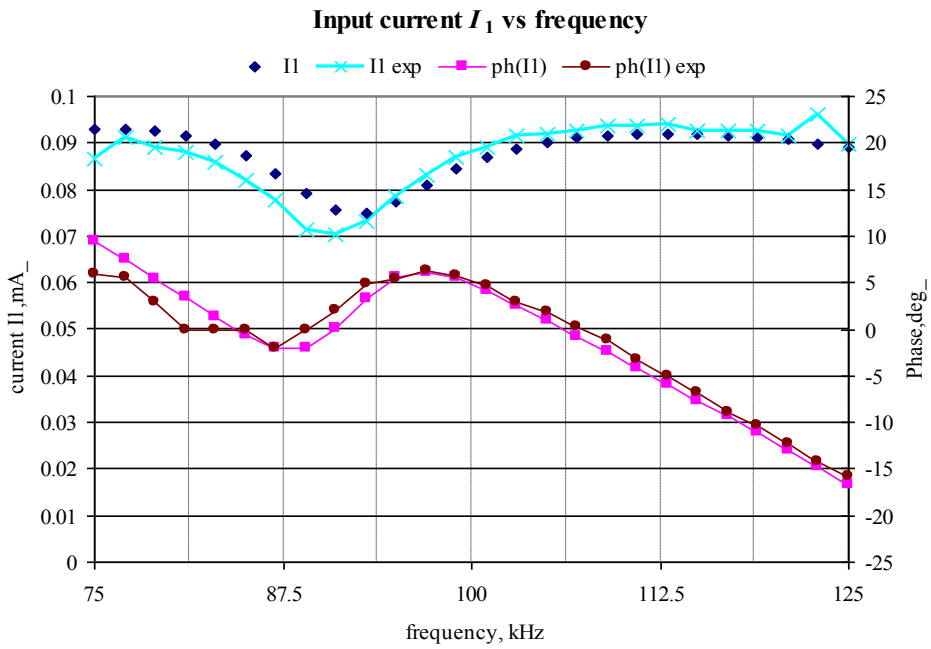

Figure 3.6: Simulated and measured input current I_1 vs. frequency. Variables labeled "exp" are measured values

Figure 3.7 compares both simulated and experimental voltage and phase of V_{L2}, as a function of frequency for the test conditions in Figure 3.4.

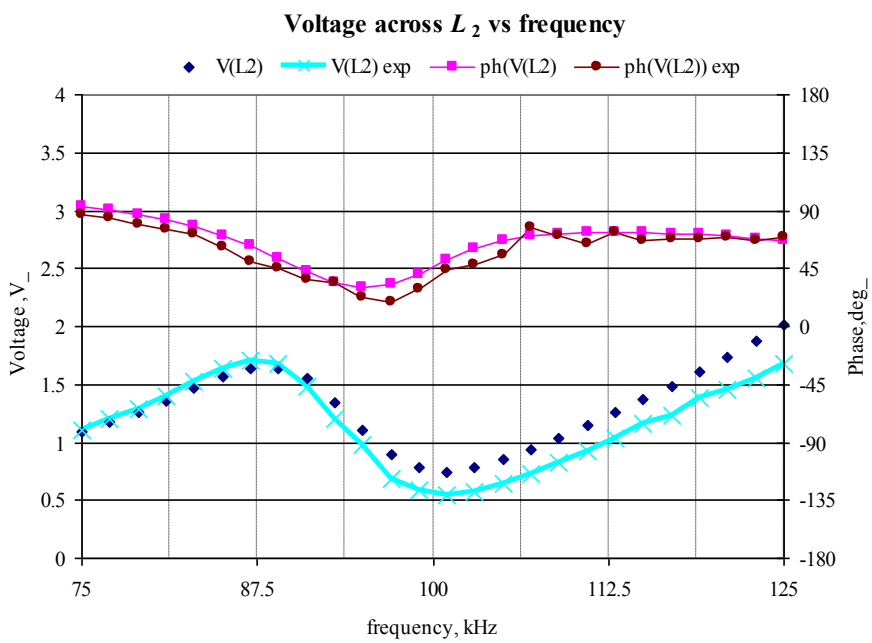

Figure 3.7: Simulated and measured voltage across L_2 vs. frequency

Figure 3.8 compares both simulated and experimental voltage and phase of V_{L3}, as a function of frequency.

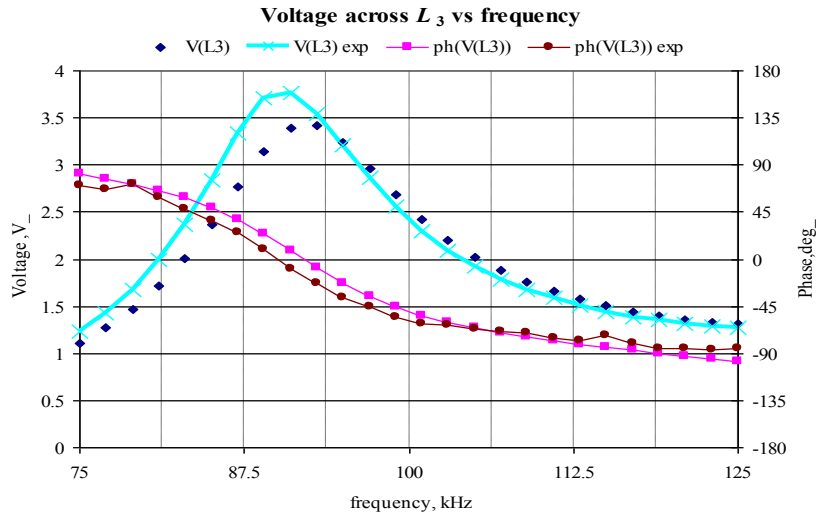

Figure 3.8: Voltage across L_3 vs. frequency

Figure 3.9 compares both simulated and experimental voltage and phase of load coil V_{RL}, as a function of frequency

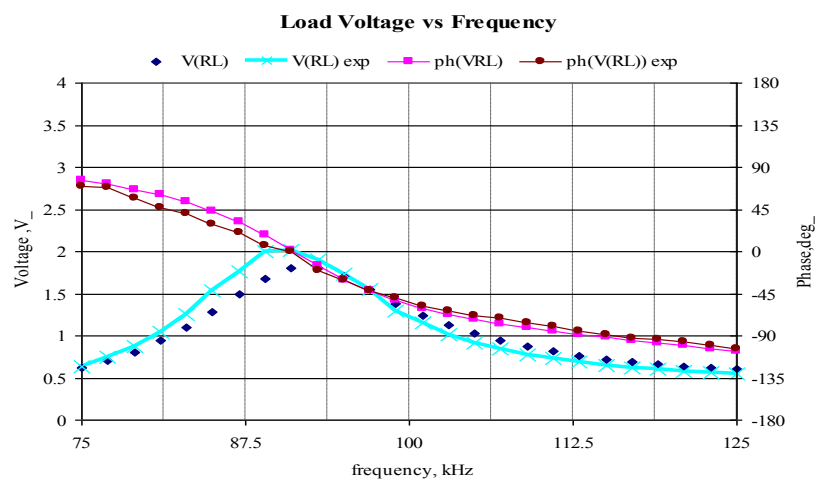

Figure 3.9: Voltage across R_L vs. frequency

It is observed from Figures 3.6–3.9, the agreement between the measured and simulated results agree quite well.

Similar experiments are conducted by changing the distance between coils L_2 and L_3 in Figure 3.4 which is D_{23} to 38.1mm and 50.8mm.

3.3.3 Experimental results with D23 =38.1mm:

Similar methodology discussed in section 3.3.1 has been followed to validate the four-coil model with D_{23} = 38.1mm in Figure 3.4 is performed and the following results were obtained.

Figure 3.10 compares simulated and measured input I_1 and phase of the current I_1 as a function of frequency.

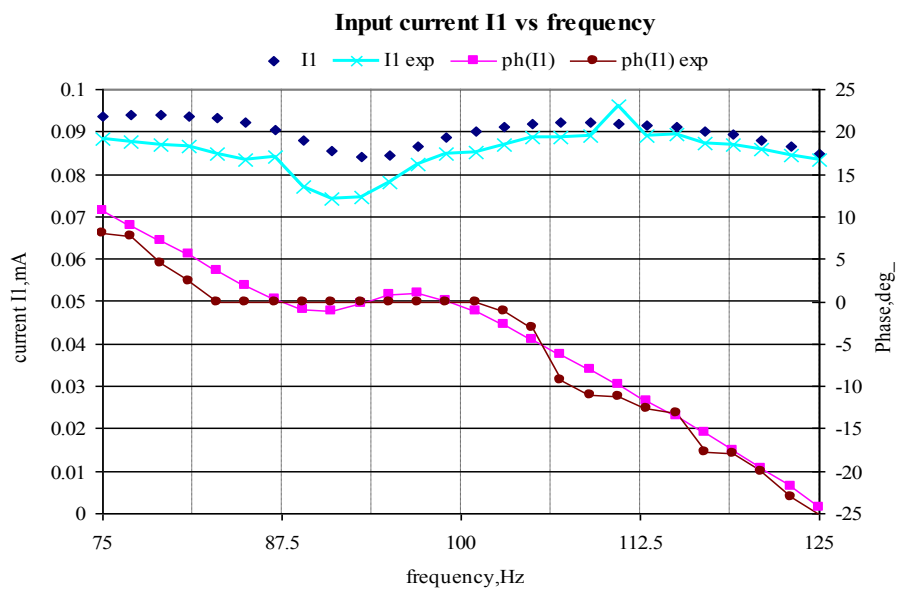

Figure 3.10: Simulated and measured input current I_1 vs. frequency. Variables labeled "exp" are measured values

Figure 3.11 compares both simulated and experimental voltage and phase of V_{L2}, as a function of frequency.

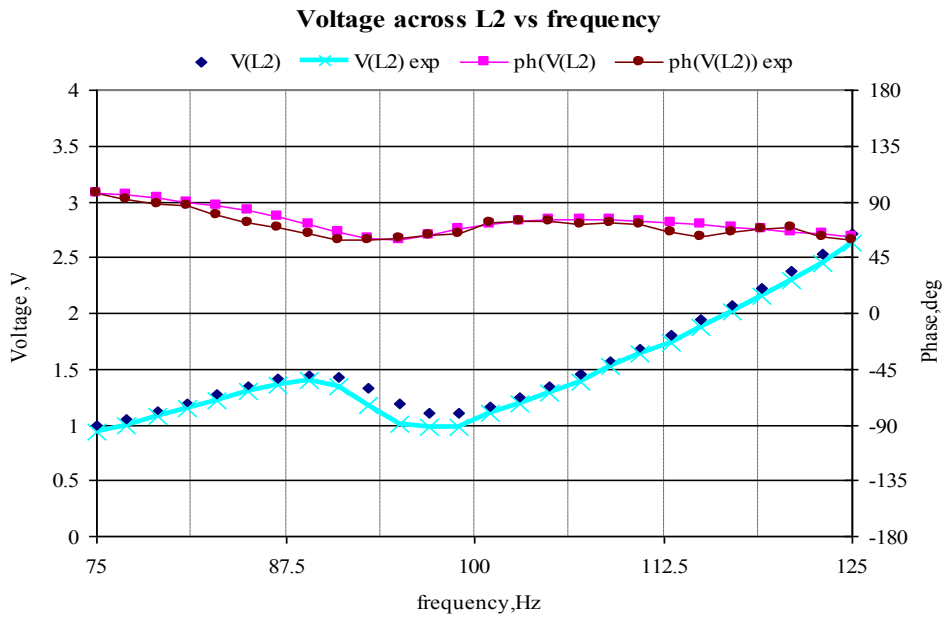

Figure 3.11: Voltage across L_2 vs. frequency

Figure 3.12 compares both simulated and experimental voltage and phase of V_{L3}, as a function of frequency.

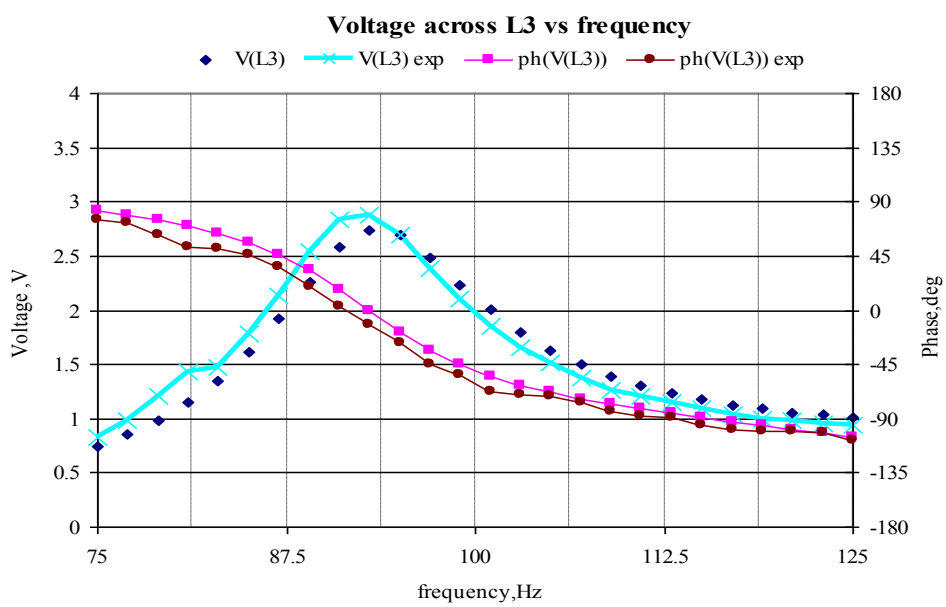

Figure 3.12: Voltage across L_3 vs. frequency

Figure 3.13 compares both simulated and experimental voltage and phase of load coil V_{RL}, as a function of frequency.

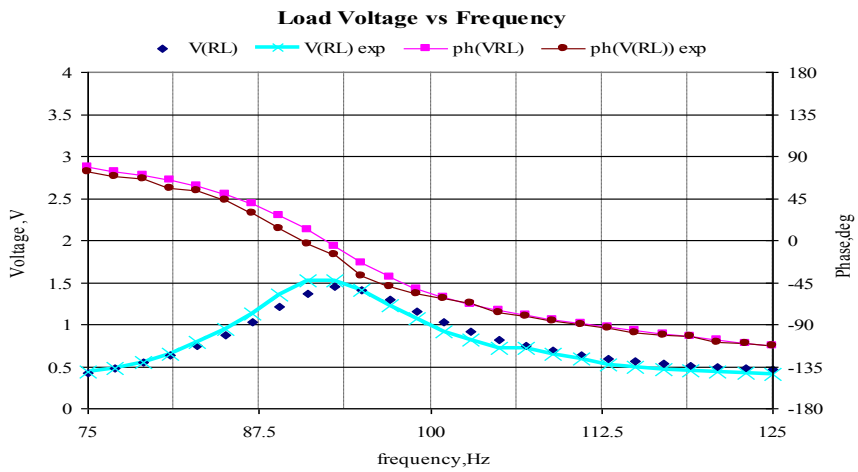

Figure 3.13: Voltage across R_L vs. frequency

3.3.4 Experimental results with D23 = 50.8mm

Similar methodology discussed in section 3.3.1 has been followed to validate the four-coil model shown in figure 3.4 with D_{23} = 50.8mm is performed and the following results were obtained.

Figure 3.14 compares simulated and measured input I_1 and phase of the current I_1 as a function of frequency.

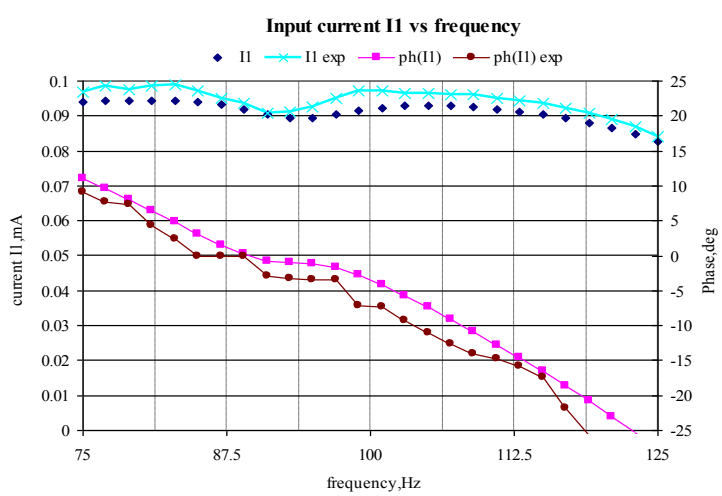

Figure 3.14: Simulated and measured input current I_1 vs. frequency. Variables labeled "exp" are measured values

Figure 3.15 compares both simulated and experimental voltage and phase of V_{L2}, as a function of frequency for the test conditions in Figure 3.4.

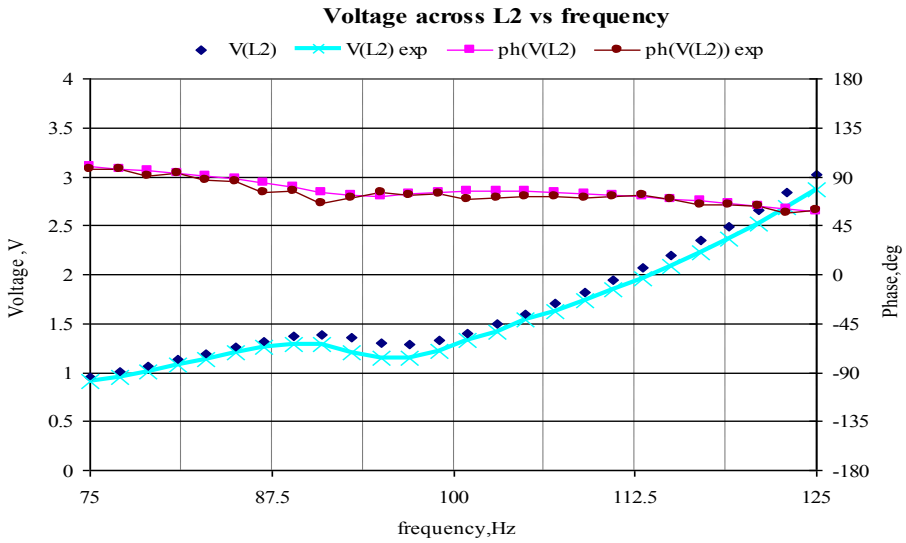

Figure 3.15: Voltage across L_2 vs. frequency

Figure 3.16 compares both simulated and experimental voltage and phase of V_{L3}, as a function of frequency.

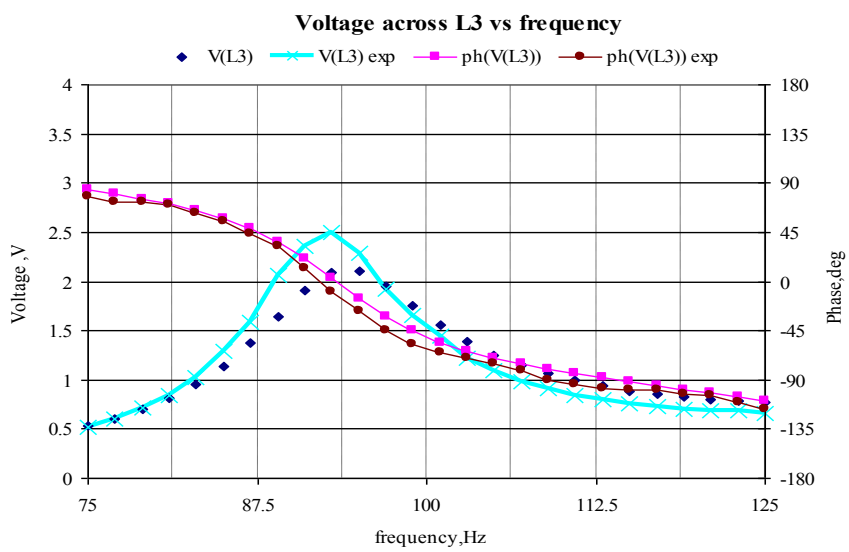

Figure 3.16: Voltage across L_3 vs. frequency

Figure 3.17 compares both simulated and experimental voltage and phase of load coil V_{RL}, as a function of frequency.

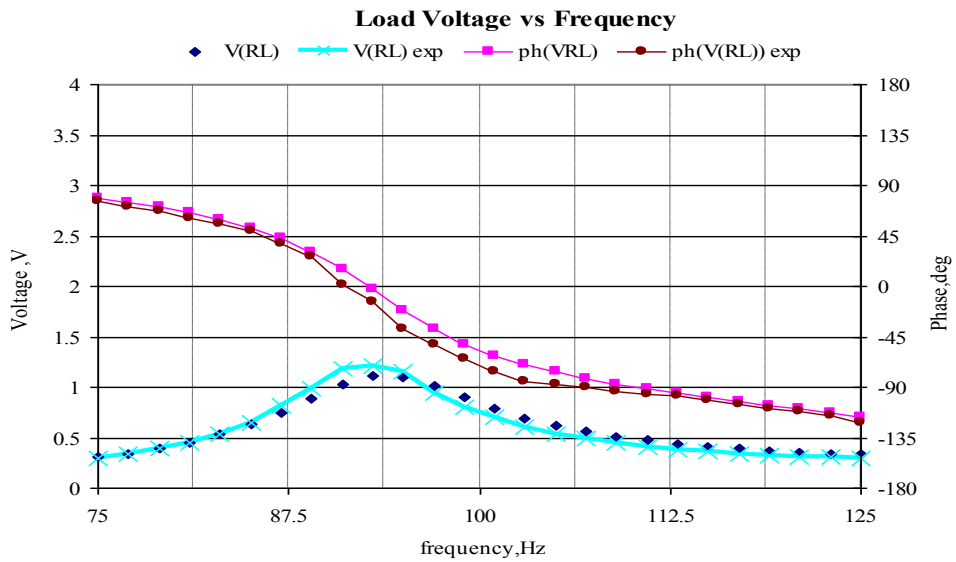

Figure 3.17: Voltage across R_L vs. frequency

3.4 Summary

It is observed from the validation experiments described in section 3.3 the simulated and measured values agree confirming the validity of the coupled resonant model of the WPT network.

Chapter Four

Calculation of mutual inductance from magnetic vector potential for WPT applications

Applications of various WPT systems involve coils of various geometries and variable orientations. Such variable geometries are often investigated through finite-element analysis (FEA). However, the method of magnetic vector potential may be employed in calculation of mutual inductance of such geometries as a substitute for FEA.

The basic structure of a four-coil WPT system is shown in Figure 4.1. Both the source and load sides of the system as drawn consist of a pair of coplanar, coaxial coils, and these coil pairs (L_1–L_2 and L_3–L_4) are shown as parallel and coaxial. This geometry is meant for illustration purposes only; in principle, arbitrary orientation of each of the four coils is possible, and geometries other than circular are also possible.

Power transmission in Figure 4.1 is principally effected by mutual inductances M_{12}, M_{23}, and M_{34}. However, the "secondary" mutual inductances M_{13}, M_{14}, and M_{24} play significant roles in the performance of the WPT system, and their presence may not be ignored.

Design of WPT systems would benefit from a tool that permits accurate computation of the mutual inductances that arise from placing coils of various forms in arbitrary positions and orientations with respect to each other.

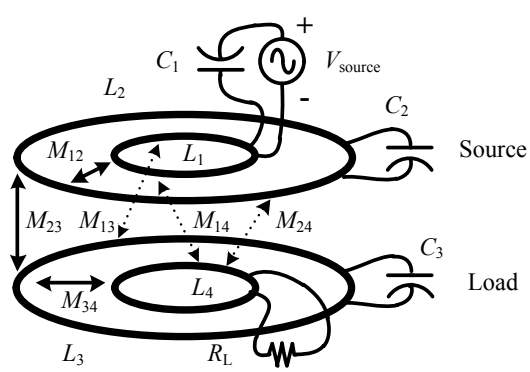

Figure 4.1: Basic four-coil WPT system.

Solid arrows in the Figure 4.1 designate principal mutual inductances for power transmission; "secondary" mutual inductances are indicated with dotted arrows.

4.1 Calculation of mutual inductance from the magnetic vector potential

Figure 4.2 below shows a current I passing through a closed path L_1, creating a magnetic flux whose density at any point is represented by $\vec{\boldsymbol{B}}$. Let $\boldsymbol{d\vec{n}}$ be a vector normal to the surface enclosed by path L_2 and having a length equal to the incremental area dn as depicted in Figure 4.2.

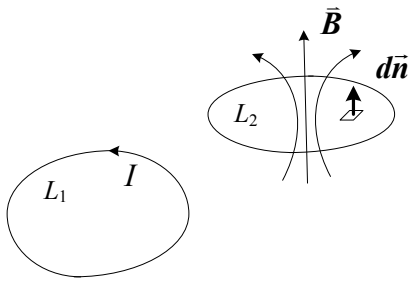

Figure 4.2: Geometry for computation of flux linkages and mutual inductance between closed paths L_1 and L_2

Some of the flux created by current I in path L_1cuts through closed path L_2 and is said to be linked to L_2. The flux linkages Λ may be computed as the surface integral of $\vec{\boldsymbol{B}} \cdot \boldsymbol{d\vec{n}}$:

$$\Lambda = \oiint_{\boldsymbol{L_2}} \vec{\boldsymbol{B}} \cdot \boldsymbol{d\vec{n}} \tag{4.1}$$

The total flux linkages to L_2 divided by current I is the mutual inductance of paths L_1 and L_2.

$$M_{12} = \frac{1}{I} \oiint_{\boldsymbol{L_2}} \vec{\boldsymbol{B}} \cdot \boldsymbol{d\vec{n}} \tag{4.2}$$

In principle, it is possible to compute the magnetic flux density $\vec{\boldsymbol{B}}$ at points interior to the path L_2 due to the current in L_1 by the Biot-Savart Law. However, Stokes' Theorem of vector calculus allows the surface integral of $\vec{\boldsymbol{B}} \cdot \boldsymbol{d\vec{n}}$ in Eq. (4.2) to be found by computing the contour integral of the curl of $\vec{\boldsymbol{B}}$ ($\nabla \times \vec{\boldsymbol{B}}$) around the path L_2, as expressed in Eq. (4.3) below:

$$\oiint_{L_2} \vec{B} \cdot d\vec{n} = \oint_{L_2} \nabla \times \vec{B} \cdot d\vec{s} \tag{4.3}$$

where $d\vec{s}$ is a vector tangent to path L_2 having a length equal to incremental length ds along path L_2.This is illustrated in Figure 4.3.Thus M_{12}, the mutual inductance of paths L_1 and L_2, may be found as:

$$M_{12} = \frac{1}{I} \oiint_{L_2} \vec{B} \cdot d\vec{n} = \frac{1}{I} \oint_{L_2} \nabla \times \vec{B} \cdot d\vec{s} \tag{4.4}$$

Define the vector quantity $\vec{A}$ (called the magnetic vector potential) as the curl of $\vec{B}$ .Then the mutual inductance may be computed by Eq. (4.5):

$$M_{12} = \frac{1}{I} \oint_{L_2} \nabla \times \vec{B} \cdot d\vec{s} = \frac{1}{I} \oint_{L_2} \vec{A} \cdot d\vec{s} \tag{4.5}$$

The geometry for computing $\vec{A}$ is depicted in Figure 4.3.

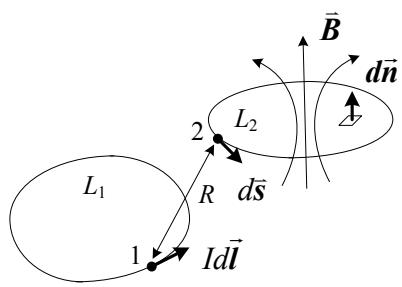

Figure 4.3: Geometry for computation of magnetic vector potential and mutual inductance

The definition $\vec{A} = \nabla \times \vec{B}$ is assumed in the following derivation. The increment of magnetic vector potential $d\vec{A}$ at point 2 on path L_2 due to the current element $Id\vec{l}$ at point 1 on path L_1 is defined as:

$$d\vec{A} = \frac{\mu_o}{4\pi R} Id\vec{l} \tag{4.6}$$

where μ_o is the magnetic permeability of free space ($4\pi\times10^{-7}$H/m) and R is the distance between points 1 and 2. The incremental flux linkages around L_2 (represented as $d\Lambda$) due to current element $Id\vec{l}$ are computed by integrating $d\vec{A} \cdot d\vec{s}$ around the closed path L_2:

$$d\Lambda = \frac{\mu_o}{4\pi} \oint_{L_2} \frac{I d\vec{\boldsymbol{l}} \cdot d\vec{\boldsymbol{s}}}{\boldsymbol{R}} \tag{4.7}$$

Integrating $d\Lambda$ due to current elements $Id\vec{\boldsymbol{l}}$ around the path L_1 allows the computation of the mutual inductance. Thus computing the mutual inductance of paths L_1 and L_2 requires computing a double integral:

$$M_{12} = \frac{1}{I} \oint_{L_1} d\Lambda = \frac{\mu_o}{4\pi\, I} \oint_{L_1} \left(\oint_{L_2} \frac{I d\vec{\boldsymbol{l}} \cdot d\vec{\boldsymbol{s}}}{\boldsymbol{R}} \right) \tag{4.8}$$

4.2. Numerical methods for calculation of mutual inductance from the magnetic vector potential

The following is a description of the methodology of computation of mutual inductance between two coils of arbitrary geometry and orientation using the principle of the magnetic vector potential outlined in Section 4.1. Numerical integration of Eq. (4.8) is the accomplished by the following process. The locus of points comprising coil L1 is represented as an n1x 3 matrix of points in Cartesian coordinates with each row being the (x,y,z) coordinates of one point on L1.

The locus of points on coil L2 is represented as an n2 x 3 matrix of points in Cartesian coordinates with each row being the (x,y,z) coordinates of one point on L2.

In the geometry shown in the Figure 4.4, ($\bar{\boldsymbol{x}}_1, \bar{\boldsymbol{y}}_1, \bar{\boldsymbol{z}}_1$) are the coordinates of the midpoint of $d\vec{\boldsymbol{l}}$ and ($\bar{\boldsymbol{x}}_2, \bar{\boldsymbol{y}}_2, \bar{\boldsymbol{z}}_2$) are the coordinates of the midpoint of $d\vec{\boldsymbol{s}}$.

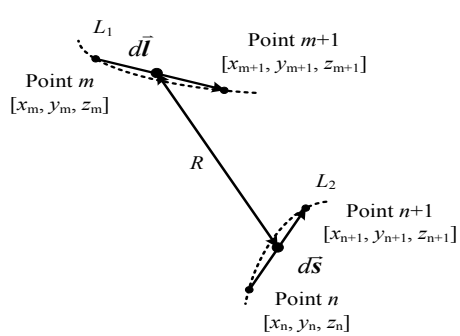

Figure 4.4: Geometry for numerical estimation of magnetic vector potential and mutual inductance

Tangent vectors ***dl*** and ***ds*** from figure 4.4 are represented by the following equations

$$\bar{\boldsymbol{x}}_1 = \frac{x_{m+1} + x_m}{2} \qquad \bar{\boldsymbol{y}}_1 = \frac{y_{m+1} + y_m}{2} \qquad \bar{\boldsymbol{z}}_1 = \frac{z_{m+1} + z_m}{2} \tag{4.9}$$

$$\bar{\boldsymbol{x}}_2 = \frac{x_{n+1} + x_n}{2} \qquad \bar{\boldsymbol{y}}_2 = \frac{y_{n+1} + y_n}{2} \qquad \bar{\boldsymbol{z}}_2 = \frac{z_{n+1} + z_n}{2} \tag{4.10}$$

$$R = \sqrt{(\bar{\boldsymbol{x}}_1 - \bar{\boldsymbol{x}}_2)^2 + (\bar{\boldsymbol{y}}_1 - \bar{\boldsymbol{y}}_2)^2 + (\bar{\boldsymbol{z}}_1 - \bar{\boldsymbol{z}}_2)^2} \tag{4.11}$$

The process of numerical integration involves the following steps:

1. Initialize the total flux linkages Λ to zero;
2. Compute the vector between the second and first points of the path $L1$, and determine the coordinates of the midpoint of ***dl*** ;
3. Compute an array of vectors ***ds*** successive pairs of points along path $L2$,and determine the coordinates of their midpoints;
4. Compute an array of dot products ***dl·ds*** for each element ***ds***;
5. Compute an array of distances R between ***dl*** and each element ***ds***;
6. Divide, element-by-element, the array of dot products from (4) by the distances R from (5);
7. Add each element of the array formed in (6) to the total of flux linkages (Λ);
8. Increment the indices of the start and end points of ***dl*** and repeat steps (2)-(7).
9. Repeat the process until the entire locus of L_1 has been traversed.
10. Multiply Λ by μo / 4π.

4.3. Computation of self-inductance with the method of magnetic vector potential:

The self-inductance of an inductor could in principle be found by computing the flux linkages from the inductor to itself. However, the method described above will encounter a divide-by-zero error if the two coils coincide at one or more points. Hence one cannot simply use the same locus points for both L_1 and L_2 in the method above (section 4.2). However, the method above may be applied if a second inductor L_1' with dimensions almost identical to the first inductor L_1 is defined and placed in tight

juxtaposition to L_1 but without touching it. Figure 4.5 shows an example of two interleaved spirals.

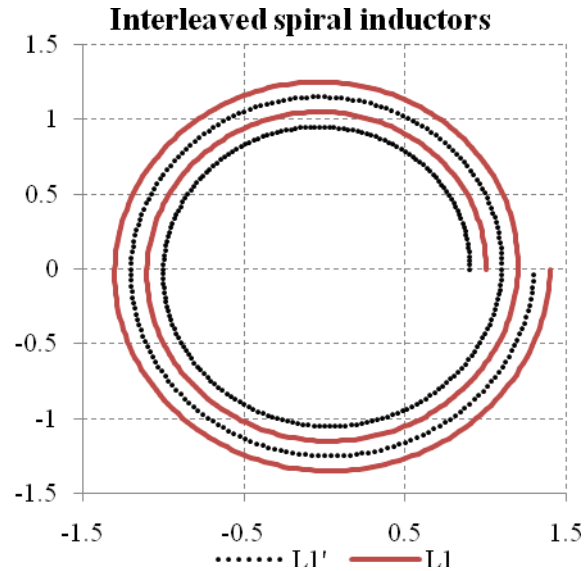

Figure 4.5: Example of interleaved inductors for applying the magnetic-vector potential method to calculation of self-inductance of a spiral coil

Close proximity of the two coils would cause virtually all flux linked from L_1 to itself to also be linked to L_1', and the self-inductance of L_1 may then be computed as the mutual inductance of L_1 and L_1'.

4.4. Empirical tests of numerical computation of self and mutual inductances

Tests have been performed to validate the computational methodology outlined in the sections 4.2 and 4.3. Two -layer solenoid coils were wound for use in the experiments described below.

The self-inductance of the solenoid coils were measured at 100 kHz using the "L_s" measurement mode of the 4362 LCR Bridge (a physical inductor is resolved into a series combination of an inductance and a resistance).

Matlab based simulators for spiral, solenoid, and rectangular coils were developed to calculate the self-inductance of respective coils using the method described in section 4.3 in which the self-inductance is calculated as the mutual inductance of the original coil with a "shadow" which is slightly rotated by 1° below the original coil.

In this case the solenoid coils are considered and their self-inductance is calculated by the Matlab simulator solenoid_creator4c. Figure 4.6 is an image of the graphical user interface (GUI) of solenoid_creator4c.

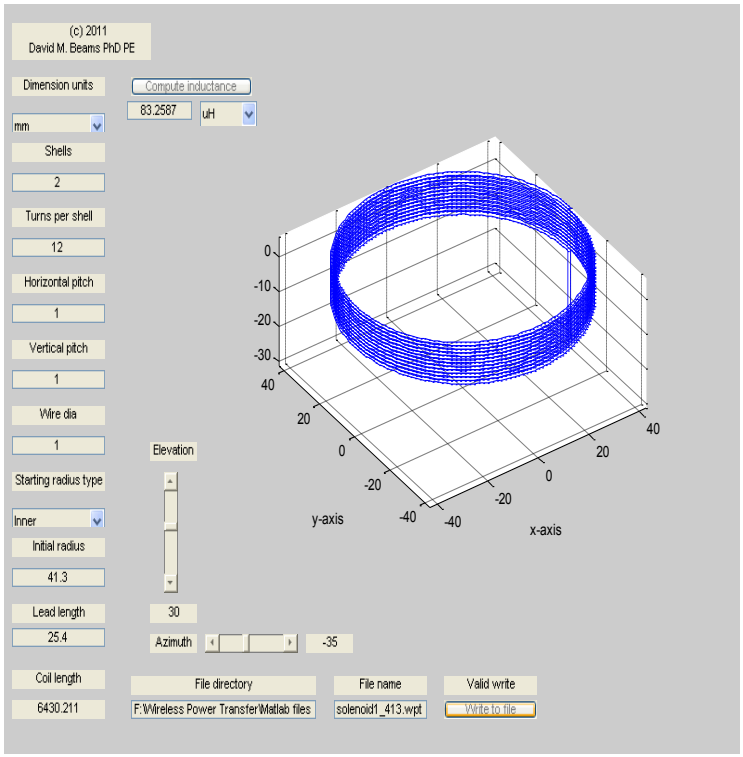

Figure 4.6: GUI of the solenoid creator

4.4.1 Experimental coil descriptions and comparison of measured and calculated self-inductances

Table 4.1 below gives a description of the two-layer solenoid coils and compares the measured and calculated self-inductance. The self-inductance was calculated by computing the mutual inductance between the coil and a “shadow” coil interleaved with the original coil.

Table 4.1: Physical description of solenoid coils used in mutual-inductance experiments

Coil	L_1	L_2
Turns	12	14
Horizontal pitch, mm	1	1
Vertical pitch, mm	1	1
Radius of inner layer, mm	41.3	41.3
Measured inductance, μH	80.3	101.2
Calculated inductance, μH	83.3	107.7
Coil file name	solenoid1_413	solenoid2_413

Hence the method for calculating self-inductance of two-layer solenoid coils is validated as the measured values are in good agreement with calculated values.

4.4.2: Measured and calculated mutual inductances between a pair of coils

Tests were conducted to validate the method of calculation of mutual inductance from magnetic vector potential method described in section 4.2. Matlab-based simulator mutual_inductance_calculator5 was developed to calculate the mutual inductance between a pair of coils. The center of each coil is assumed to be at the origin (0,0,0) of a system of Cartesian coordinates and the central axis of the coil is assumed to be the *z*-axis. However, the simulator allows each coil to be rotated around any axis, and the center of the coil may be displaced with user-supplies displacements in *x*-ory- or z-directions. Roll denotes rotation about the *x*-axis, pitch about the *y*-axis and yaw about

the z-axis. Each rotation angle is defined according to the right-hand rule (with the thumb extended in the positive axis direction, the curl of the fingers positive rotation).

Coils were arranged coaxially with coil planes parallel to each other as shown in Figure 4.7 and the mutual inductance between them was measured at 100 kHz using the "L_s" measurement mode of the HP 4362 LCR Bridge. Mutual inductances were determined by measuring the total inductance of the coils connected in series-aiding and in series-opposing connection. Denoting total inductance in series-aiding connection by L_{S+} and total inductance in series-opposing connection at L_{S-}, the mutual inductance M is given by:

$$M = \frac{L_{S+} - L_{S-}}{4} \tag{4.12}$$

Computed mutual inductances were calculated with Matlab program mutual_inductance5.m. The coils as described in their files included short lead connections; the coil entered as coil 2 in the simulator was rotated 180º in the roll axis so that its leads pointed upward, away from coil 1. Coil center-to-center spacing was entered as z-axis displacement of coil 2. No x- or y-axis displacements or pitch and yaw displacements were entered for coil 2.Figure 4.7 below is an image of the graphical user interface (GUI) of the mutual inductance calculator with a center-to-center vertical spacing of 7.7cm between the coils.

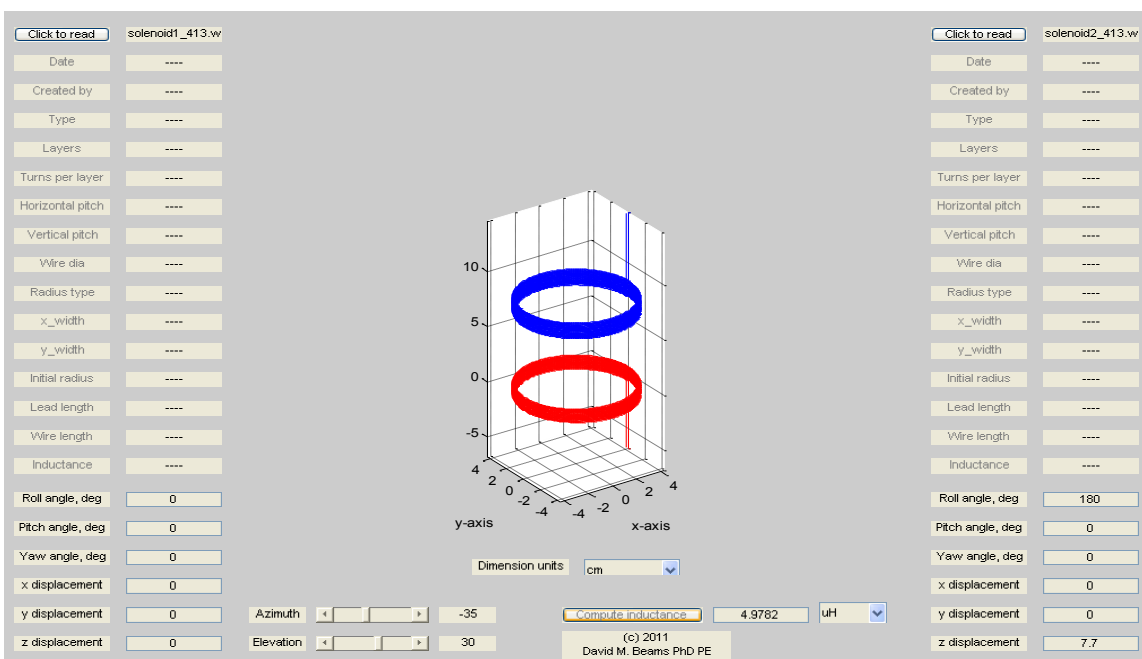

Figure 4.7:GUI of Matlab mutual inductance calculator

The measured and computed inductances with respective center-to-center spacing for experiments of 13 April 2011 are tabulated below.

Table 4.2: Measured vs. computed mutual inductance

Center-to-center spacing, cm	Measured mutual inductance, μH	Computed mutual inductance, μH
7.7	4.82	4.98
8.7	3.72	3.84
9.7	2.92	3.00
10.7	2.32	2.39
12.7	1.60	1.57

Measured mutual inductance values which are approximately closer to those of calculated values with respective coil-coil spacing (shown in Table 4.2) validates the method of computing mutual inductance using magnetic vector potential method.

4.5 Application to inductors backed by ferrite

One possible configuration of WPT systems uses high-permeability ferrite material as a backing for each pair of inductors. The principal benefit is to confine fluxes to the region between the inductors and reduce unintentional coupling of magnetic flux to nearby objects.

It was conjectured that the computation of mutual inductances with magnetic vector potential might still be feasible for inductors "sandwiched" between ferrite sheets if flux linkages due to image currents in the ferrite sheets are included. Figure 4.8 shows how this might be applied to finding the mutual inductance between inductors L_A and L_B which are positioned above a ferrite sheet. Inductor L_A is assumed to be carrying a current I. Inductor L_A creates a reflection (or image) in the ferrite sheet; this image coil in turn produces flux linkages to L_B. The flux created by the reflection is that produced by a

current of $I \times (\mu_r - 1)/(\mu_r + 1)$ where μ_r is the relative magnetic permeability of the ferrite material. The flux linked from inductor L_A to inductor L_B in proximity to the ferrite sheet is the sum of the linkages from L_A to L_B and the linkages from the image of L_A to L_B.

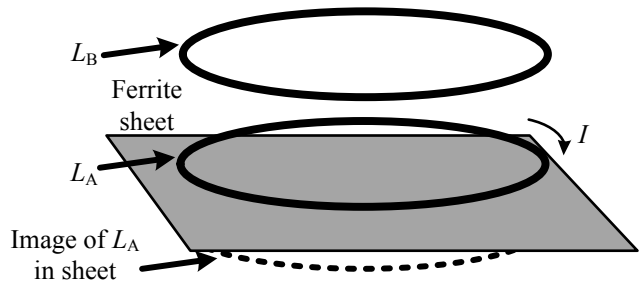

Figure 4.8: Inductors L_A and L_B positioned above a sheet of high-permeability ferrite material

An experiment was conducted to test the validity of this image method for computing mutual inductances in the presence of a ferrite sheet. Two solenoid inductors were mounted coaxially with their bottom edges aligned as shown in the Figure 4.9. The inductors were positioned at various heights above a sheet of ferrite material by means of plastic spacers.

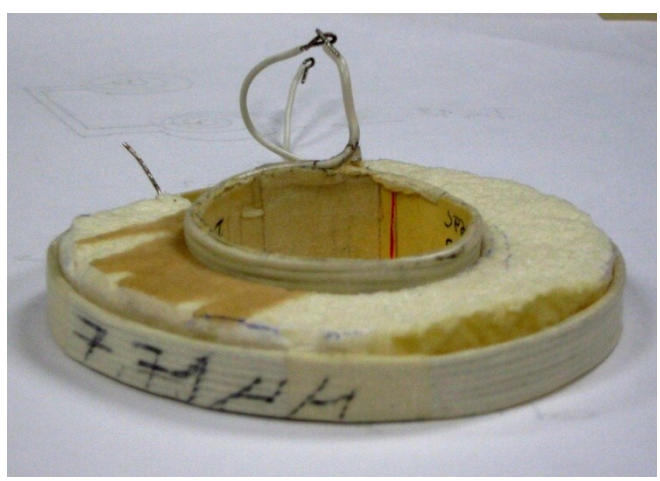

Figure 4.9: Solenoid coils mounted coaxially

The mutual inductance was measured as a function of spacing between the bottom edges and the ferrite sheet below the inductors at 100 kHz with a Hewlett-Packard 4263B *LCR* meter and the mutual inductance was computed by the image method for various spacing.

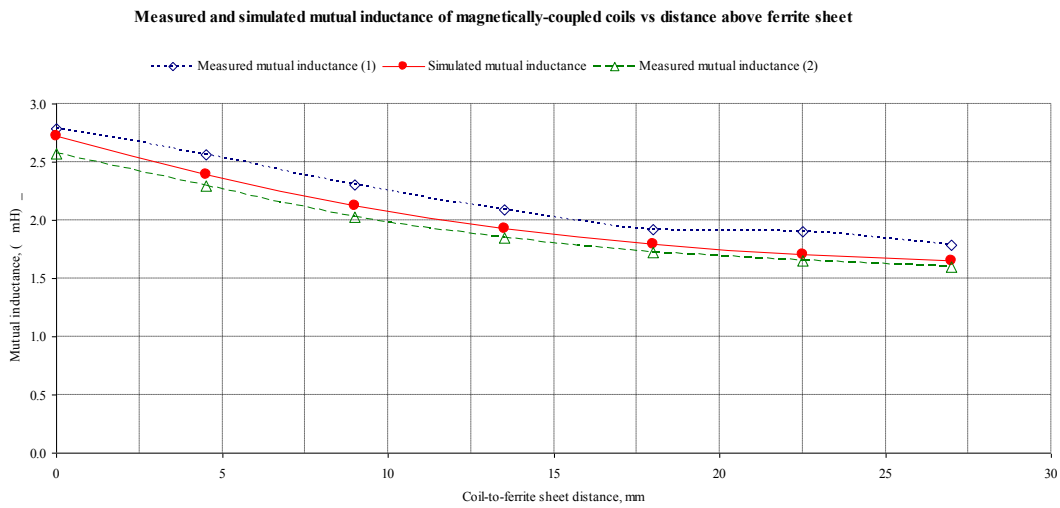

Figure 4.10: Simulated and measured results for mutual inductance between two solenoid coils vs. height over a ferrite sheet (Two separate sequences of measurements were made on two successive days).

The values and the shape of the curves in Figure 4.10 appear to confirm the validity of the image method in determination of mutual inductance of two coils in the presence of a coplanar ferrite sheet.

4.5.1 Experiment in simulating inductance of a coil in proximity to two ferrite sheets

Another set of experiments was performed to determine how the inductance of a single coil would change in the presence of two parallel ferrite sheets. A spiral-wound coil was created with the following parameters (Table 4.3) for these tests. Inductance of the spiral coil are measured using the Matlab simulator Mutual_inductance_calculator5 and are measured at 100 kHz with a Hewlett-Packard 4263B *LCR* meter.

Table 4.3: Spiral coil description used in presence of two ferrite sheets

Coil	L_1
Type	Spiral
Turns	10
Horizontal pitch, mm	1.44
Initial radius, mm	18.25
Radius type	Inner
Measured inductance, μH	6.47
Calculated inductance, μH	7.28
Coil file name	Ndack_Thierry_16JUN

The coil was positioned above a ferrite sheet with a 4.5mm foam-core spacer. Given the wire diameter (1.4mm), the spacing of the wire center to the ferrite sheet was thus 5.2mm. One or more foam-core spacers were placed atop the coil, and the second ferrite sheet was placed atop these spacers. The inductance of the coil was measured for each thickness of these spacers atop the coil. The sheet-to-sheet spacing is 4.5mm × (n+1)+ 1.4mm, where n is the number of spacers atop the coil and 1.4mm is the diameter of the wire. The geometry is shown in Figure 4.11 below.

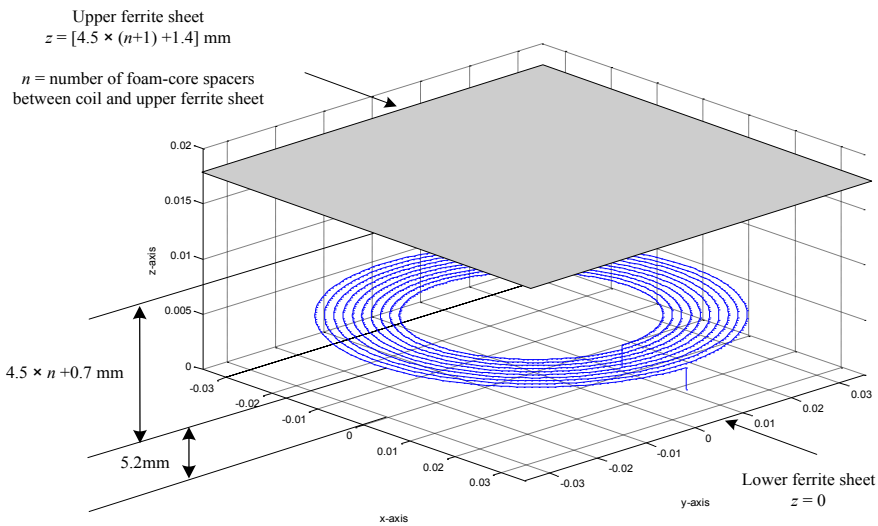

Figure 4.11: Geometry for experiments for determining the inductance of a spiral-wound coil between ferrite sheets

Inductance was computed using the image method as follows:

$$L_{\text{total}} = L_{\text{self}} + M_{\text{c,image1}} + M_{\text{c,image2}} + M_{\text{c,image12}} + M_{\text{c,image21}} \tag{4.13}$$

where:

L_{total} is the inductance of the coil between ferrite sheets;

L_{self} is the self-inductance of the coil in free space;

$M_{\text{c,image1}}$ is the mutual inductance between the coil and its image in sheet 1 (lower ferrite sheet);

$M_{\text{c,image2}}$ is the mutual inductance between the coil and its image in sheet 2 (upper ferrite sheet);

$M_{\text{c,image12}}$ is the mutual inductance between the coil and the image in sheet 1 reflected into sheet 2;

$M_{\text{c,image21}}$ is the mutual inductance between the coil and the image in sheet 2 reflected into sheet 1.

The terms $M_{\text{c,image12}}$ and $M_{\text{c,image21}}$ thus arise from multiple reflections (as in the same way that a light source between two mirrors gives rise to multiple reflections).

Figure 4.12 compares simulated inductance to measured inductance; it also shows the simulated inductance if the multiple reflections were not included. Data for this experiment were recorded in an Excel spreadsheet and displayed in graphical form..

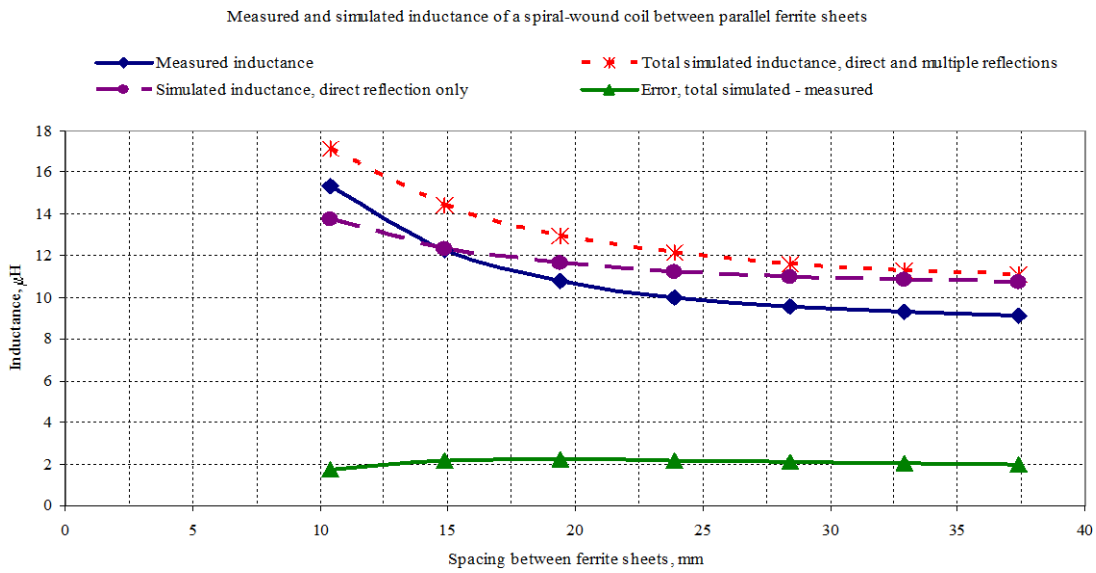

Figure 4.12: Measured and simulated inductance of a spiral-wound coil between ferrite sheets

The form of the simulated curve follows the measured curve when the multiple reflections are included; including only the first-order reflections (direct images of the coil in sheets 1 and 2) causes underestimation of simulated inductance at smaller sheet-to-sheet spacings. The error between the total simulated and measured inductances was almost constant at approximately 2 μH; approximately 40% of the error may be attributed to a disparity between the simulated self-inductance (7.285 μH) and the measured self-inductance (6.47 μH).

4.6 Summary

Numerical computation of self- and mutual inductances by magnetic vector potential methods is validated using the developed Matlab coil-design tools for various geometries (spiral, solenoid, rectangular) and demonstrated the capability to numerically compute mutual inductance between coils of arbitrary geometries in free space.

Chapter Five

Design of WPT systems by reflected impedances in loosely-coupled inductors

The four-coil WPT system has been shown to transfer electric power over short distances with high efficiency by means of loosely-coupled inductors and resonating capacitors. However, there are many degrees of freedom and many variables to manipulate, and the complexity of the design space makes *a priori* design difficult. The design method outlined in this chapter is intended to reduce that complexity by identifying the most-important design parameters and to provide a theoretical basis for experimental observations.

5.1 WPT system model:

The network shown in Figure 5.1 represents a typical four-coil WPT system. The nomenclature of the system follows Figure 5.1.

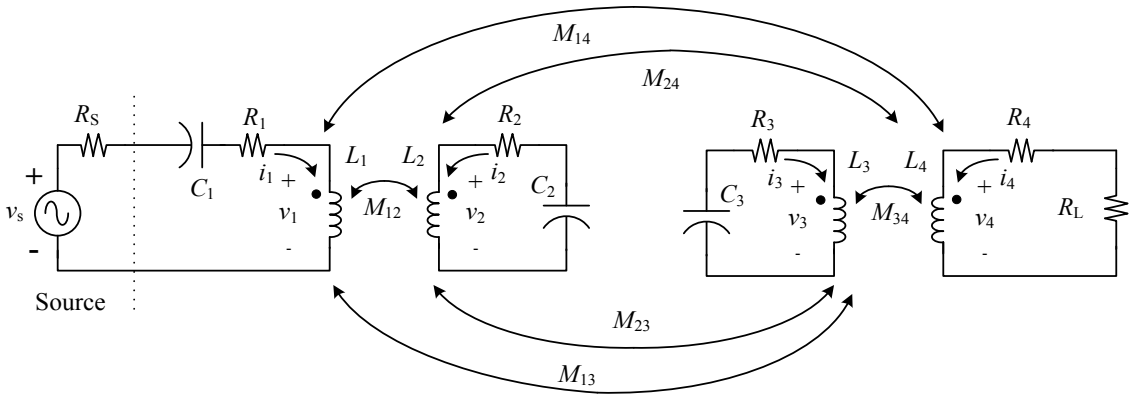

Figure 5.1: Coupled-inductor model for resonant wireless power-transfer system

v_s is a sinusoidal source voltage, V;

R_S is the output resistance of the sinusoidal source, Ω;

L_1 is the non-resonant (driven) primary winding, H;

v_1 is the voltage across L_1, V;

i_1 is the current in L_1, A;

C_1 is the coupling (dc block) capacitor between L_1 and v_s;

R_1 is the sum of the equivalent-series resistances (ESRs) of L_1 and C_1, Ω;

L_2 is the resonant primary winding, H;

v_2 is the voltage across L_2, V;

i_2 is the current in L_2, A;

C_2 is the resonating capacitor for L_2, F;

R_2 is the sum of the ESRs of L_2 and C_2, Ω;

L_3 is the resonant secondary winding, H;

v_3 is the voltage across L_3, V;

i_3 is the current in L_3, A;

C_3 is the resonating capacitor for L_3, F;

R_3 is the sum of the ESRs of L_3 and C_3, Ω;

L_4 is the non-resonant (pickup) secondary winding, H;

v_4 is the voltage across L_4, V;

i_4 is the current in L_4, A;

R_4 is the ESR of L_4, Ω;

$R_L$is the resistive load, Ω;

M_{12} is the mutual inductance between L_1 and L_2;

M_{13} is the mutual inductance between L_1 and L_3;

M_{14} is the mutual inductance between L_1 and L_4;

M_{22} is the mutual inductance between L_2 and L_3;

M_{24} is the mutual inductance between L_2 and L_4;

M_{34} is the mutual inductance between L_3 and L_4.

Equations (5.1)–(5.8) describe the system of Figure 5.1 under steady-state excitation by a sinusoidal voltage at angular frequencyω:

$$v_1 = j\omega L_1 i_1 + j\omega M_{12} i_2 + j\omega M_{13} i_3 + j\omega M_{14} i_4 \tag{5.1}$$

$$v_2 = j\omega M_{12} i_1 + j\omega L_2 i_2 + j\omega M_{23} i_3 + j\omega M_{24} i_4 \tag{5.2}$$

$$v_3 = j\omega M_{13} i_1 + j\omega M_{23} i_2 + j\omega L_3 i_3 + j\omega M_{34} i_4 \tag{5.3}$$

$$v_4 = j\omega M_{14} i_1 + j\omega M_{24} i_2 + j\omega M_{34} i_3 + j\omega L_4 i_4 \tag{5.4}$$

$$v_s = \left(R_1 + R_S \frac{1}{j\omega C_1} \right) i_1 + v_1 \tag{5.5}$$

$$v_2 = -\left(R_2 + \frac{1}{j\omega C_2} \right) i_2 \tag{5.6}$$

$$v_3 = -\left(R_3 + \frac{1}{j\omega C_3} \right) i_3 \tag{5.7}$$

$$v_4 = -(R_4 + R_L) i_4 \tag{5.8}$$

Eqs. (5.1)− (5.8) may be expressed in matrix form as:

$$\begin{bmatrix} j\omega L_1 & j\omega M_{12} & j\omega M_{13} & j\omega M_{14} & -1 & 0 & 0 & 0 \\ j\omega M_{12} & j\omega L_2 & j\omega M_{23} & j\omega M_{24} & 0 & -1 & 0 & 0 \\ j\omega M_{13} & j\omega M_{23} & j\omega L_3 & j\omega M_{34} & 0 & 0 & -1 & 0 \\ j\omega M_{14} & j\omega M_{24} & j\omega M_{34} & j\omega L_4 & 0 & 0 & 0 & -1 \\ R_1 + R_S + \frac{1}{j\omega C_1} & 0 & 0 & 0 & 1 & 0 & 0 & 0 \\ 0 & R_2 + \frac{1}{j\omega C_2} & 0 & 0 & 0 & 1 & 0 & 0 \\ 0 & 0 & R_3 + \frac{1}{j\omega C_3} & 0 & 0 & 0 & 1 & 0 \\ 0 & 0 & 0 & R_4 + R_L & 0 & 0 & 0 & 1 \end{bmatrix} \times \begin{bmatrix} i_1 \\ i_2 \\ i_3 \\ i_4 \\ v_1 \\ v_2 \\ v_3 \\ v_4 \end{bmatrix} = \begin{bmatrix} 0 \\ 0 \\ 0 \\ 0 \\ v_s \\ 0 \\ 0 \\ 0 \end{bmatrix} \tag{5.9}$$

Analysis of the system in Eq. (5.9) with tools such as Matlab or Excel is straightforward if the circuit parameters are provided. However, the application of this system to the problem of design is considerably less clear. Simplification of the design space, however, is possible if certain essential parameters are identified and if the principle of reflected impedances in mutually-coupled inductors is applied.

5.2 Reflected impedance in mutually-coupled inductors with *RC* termination

In the circuit (Figure 5.2), a voltage source v_a is connected to the terminals of an inductor L_a which coupled magnetically (with mutual inductance M_{ab}) to a second inductor L_b whose terminals are connected to a series network consisting of a capacitor C_b and a resistor R_b.

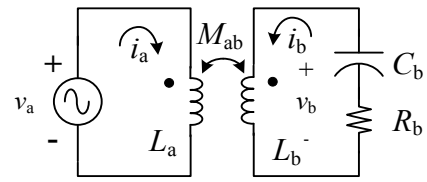

Figure 5.2: Coupled inductors with *RC* secondary termination and voltage source primary excitation

The equations relating inductor terminal voltages v_a and v_b to inductor currents i_a and i_b are:

$$\begin{aligned} v_a &= j\omega L_a i_a + j\omega M_{ab} i_b \\ v_b &= j\omega M_{ab} i_a + j\omega L_b i_b \\ v_b &= -\left(R_b + \frac{1}{j\omega C_b}\right) i_b \end{aligned} \tag{5.10a,b,c}$$

From these equations, the relationship of i_b to i_a and the impedance z_a presented to voltage source v_a may be derived:

$$i_b = i_a \left(\frac{\omega^2 M_{ab} C_b}{1 - \omega^2 L_b C_b + j\omega C_b R_b} \right) \tag{5.11}$$

$$z_a = \frac{v_a}{i_a} = \frac{-\omega^2 L_a C_b R_b + j\omega \left[L_a + \omega^2 C_b \left(M_{ab}{}^2 - L_a L_b \right) \right]}{1 - \omega^2 L_b C_b + j\omega C_b R_b} \tag{5.12}$$

The impedance of L_a can be separated into a real component R_{ref} and an imaginary component X:

$$z_a = \frac{v_a}{i_a} = R_{ref} + jX \tag{5.13a}$$

where:

$$R_{ref} = \frac{\omega^4 C_b{}^2 R_b M_{ab}{}^2}{\left(1 - \omega^2 L_b C_b\right)^2 + \left(\omega C_b R_b\right)^2} \tag{5.13b}$$

$$X = \frac{\omega L_a + \omega^3 C_b\left(M_{ab}{}^2 - 2L_a L_b + L_a C_b R_b{}^2\right) + \omega^5 C_b{}^2 L_b\left(L_a L_b - M_{ab}{}^2\right)}{\left(1-\omega^2 L_b C_b\right)^2 + \left(\omega C_b R_b\right)^2} \tag{5.13c}$$

The real component of the impedance of L_a is a reflected resistance; in the absence of mutual inductance, there is no reflected resistance and inductor L_a manifests only reactance. The reactance X, however, consists of the reactance of L_a and a reflected reactance X_{ref}. This is shown in Figure 5.3 below.

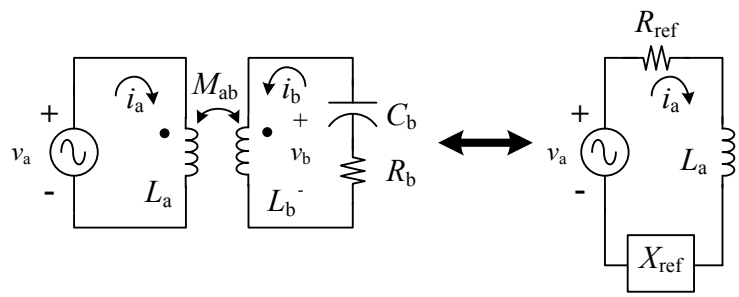

Figure 5.3: Equivalence of mutually-coupled inductors with *RC* termination and a single coil with reflected resistance R_{ref} and reactance X_{ref}

Computation with Eq. (5.13b) shows that the reflected resistance R_{ref} reaches a maximal value equal to $\omega^2 M_{ab}{}^2 / R_b$ at resonance of L_b and C_b, i.e., at $\omega = (L_b C_b)^{-(1/2)}$.

The total reactance X of impedance z_a may be expressed as:

$$X = \omega L_a + X_{ref} \tag{5.14a}$$

where:

$$X_{ref} = \frac{\omega^3 C_b\left(1-\omega^2 L_b C_b\right) M_{ab}{}^2}{\left(1-\omega^2 L_b C_b\right)^2 + \left(\omega C_b R_b\right)^2} \tag{5.14b}$$

Equation (5.14b) indicates that X_{ref} will be positive (i.e., inductive) for $\omega < (L_b C_b)^{-(1/2)}$ and negative (i.e., capacitive) for $\omega > (L_b C_b)^{-(1/2)}$. If the mutual inductance M_{ab} is sufficiently large, it is possible that the total reactance X might disappear at some frequency or even become capacitive over a range of frequencies.

Figures 5.4, 5.5, and 5.6 show the resistive and reactive components of z_a for $L_a = 25\mu H$, $L_b = 40\mu H$, $C_b = 63.32nF$, and $R_b = 3.5\Omega$, and the cases of $k_{ab} = 0.2$, 0.4, and 0.6. Also shown in these figures for comparison is the reactance of inductor L_a in isolation ($k_{ab} = 0$). Regardless of the value of flux-coupling coefficient k_{ab}, the resistive component of the input impedance z_a reaches a maximal value at a frequency corresponding to the resonance of L_b and C_b as indicated by Eq. (5.13b). However, as also demonstrated by Eq. (5.13b), the maximal resistance is affected strongly by the mutual inductance, which is proportional to the value of the flux-coupling coefficient. For frequencies close to but less than the resonance of L_b and C_b, the reactance of z_a is an inductive reactance exceeding that of L_a alone; however, for frequencies above resonance of L_b and C_b, the reactance falls below that of L_a, and it is possible with sufficient flux coupling for the reactance of z_a to become capacitive, as observed in Figure 5.6. This behavior is in accordance with Eq. (5.14b).

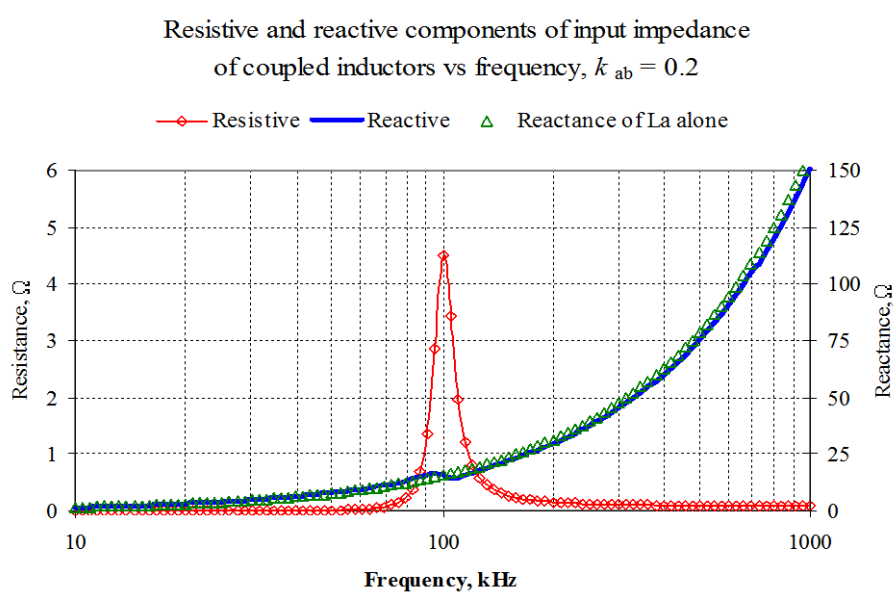

Figure 5.4: Resistive and reactive components of the input impedance at the terminals of L_a for values specified and for $k_{ab} = 0.2$.

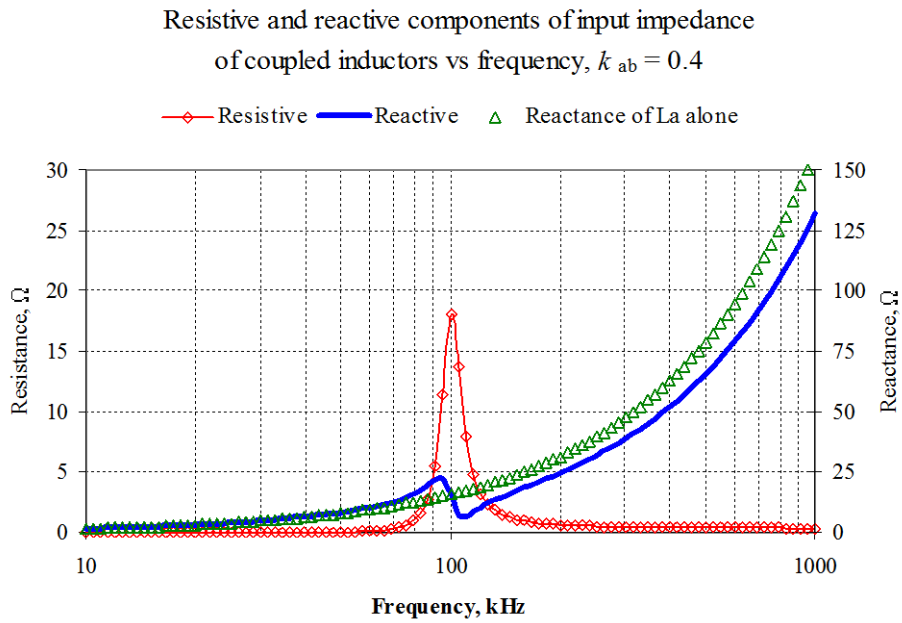

Figure 5.5: Resistive and reactive components of the input impedance at the terminals of L_a for values specified and for $k_{ab} = 0.4$

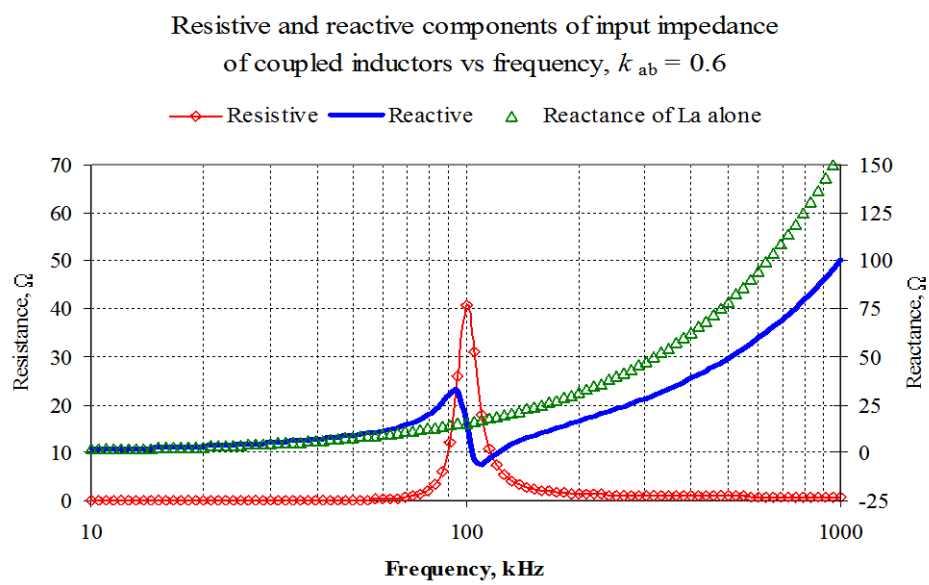

Figure 5.6: Resistive and reactive components of the input impedance at the terminals of L_a for values specified and for $k_{ab} = 0.6$. It is noted that the reactive component of the input impedance is capacitive for frequencies just above the resonance peak.

The radian resonant frequency of L_b and C_b can be defined as ω_o

$$\omega_o = \frac{1}{\sqrt{L_b C_b}} \tag{5.15}$$

Substitution for ω_o for ω in Eq. (5.11) gives the relationship of current i_b to i_a at the resonant frequency of L_b and C_b:

$$i_b = i_a \left(\frac{-j\omega_o M_{ab}}{R_b} \right) \tag{5.16}$$

Thus i_b is seen to be in phase quadrature with i_a, having a phase of –90° with respect to i_a. Substitution of ω_o for ω in Eq. (5.12) gives an expression for the input impedance of $L_a$at the resonant frequency of L_b and C_b:

$$\frac{v_a}{i_a}(j\omega_o) = j\omega L_a + \frac{(\omega_o M_{ab})^2}{R_b} \tag{5.17}$$

The reactance of L_a at ω_o is the same as it would have been considering only the self-inductance of L_a; however, a resistive component is reflected into L_a from L_b proportional to the square of the mutual inductance M_{ab} and inversely proportional to R_b.

5.3 Reflected impedance in mutually-coupled inductors with resistive termination:

An example of coupled inductors with resistive termination is shown in Figure 5.7 as in the case of coupled inductors with *RC* termination, the impedance manifested at the terminals of $L_a$will contain a reflected resistance R_{ref} and a reflected reactance X_{ref}.

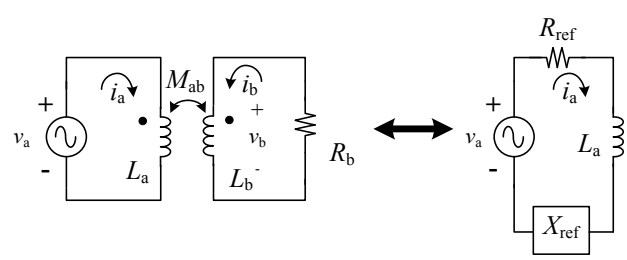

Figure 5.7: Mutually-coupled inductors with resistive termination

The values of reflected resistance and reflected reactance can be derived from Eqs. (5.13b) and (5.14b) respectively, by allowing the capacitance of C_b to approach an infinite value (thus producing a reactance that approaches zero). So doing yields expressions for reflected resistance and reactance for coupled inductors with resistive termination:

$$R_{\text{ref}} = \frac{\omega^2 R_b M_{ab}^2}{\omega^2 L_b^2 + R_b^2} \tag{5.18a}$$

$$X_{\text{ref}} = \frac{-\omega^3 L_b M_{ab}^2}{\omega^2 L_b^2 + R_b^2} \tag{5.18b}$$

Comparison of Eq. (5.18a) for R_{ref} with Eq. (5.13b), the equivalent expression for the case of RC termination, shows that for resistive termination R_{ref} approaches a limit of $R_b M_{ab}^2 / L_b$ if $\omega L_b >> R_b$. Equation (5.18b) shows that the coupled reactance is always negative (i.e., capacitive) for the case of resistive termination but that the limiting value of the coupled reactance is $-\omega L_a$, a value that is approached only when $\omega L_b >> R_b$ (the termination of L_b approaches a short-circuit) and $M_{ab}^2 = L_a L_b$ (i.e., for perfect flux coupling between L_a and L_b). This latter condition is not typical of WPT systems; hence the input impedance of L_a in a WPT system will always contain inductive reactance.

The relationship of current i_b to current i_a is:

$$i_b = \frac{-j\omega M_{ab}}{R_b + j\omega L_b} i_a \tag{5.19}$$

Equation (5.19) gives the relation between the currents i_b and i_a showing the input impedance of L_a in a WPT system will have negative reactance in which the current i_b will lag i_a by some angle between –90° (limiting case when $R_b >> \omega L_b$) to –180° (when $\omega L_b >> R_b$).

5.4 Application of reflected impedances to the analysis of a four-coil WPT system:

Inductor L_1 and series capacitor C_1 form the input network for the WPT system. When all mutual couplings are taken into account, the WPT system may be collapsed to an equivalent network as shown in Figure 5.8.

The analysis which follows has as its aim to develop an expression that allows calculation of reflected resistances and reactances into L_1. The reflected resistance that arises from load resistor R_L is the resistance to which useful power is delivered by the sinusoidal voltage source; reflected resistance in L_1 arising from resistive loss elements in the WPT system will reduce the efficiency of power transfer from the source to the load. For purposes of this analysis, it will be assumed that the important mutual inductances are M_{12}, M_{23}, and M_{34}. This simplifies the model to make it tractable for hand analysis; the validity of this assumption may be tested later by simulation.

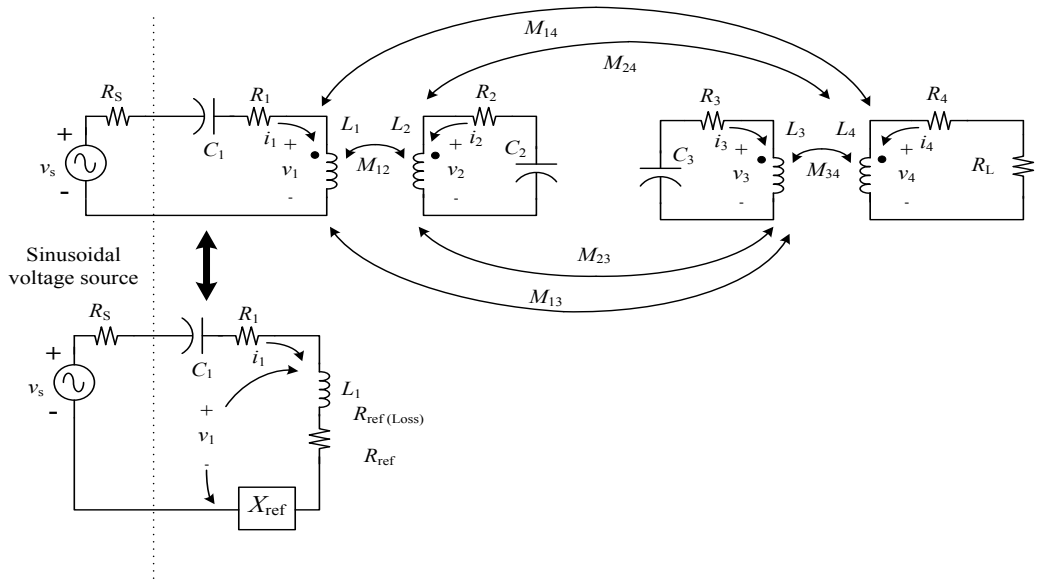

Figure 5.8: Proposed equivalent circuit reducing a four-coil WPT system to a single-loop circuit including reflected resistances and reactances.

Parasitic resistance R_4 and load resistance R_L form the composite load for L_4 which is coupled to L_3. At angular operating frequency ω_o, a resistance R_{ref34} and a reactance X_{ref34} are reflected into L_3 as given in Eqs. (5.20a) and (5.20b):

$$R_{\text{ref}34}(\omega_o) = \frac{\omega_o^2 (R_4 + R_L) M_{34}^2}{\omega_o^2 L_4^2 + (R_4 + R_L)^2} \tag{5.20a}$$

$$X_{\text{ref}34}(\omega_o) = \frac{-\omega_o^3 L_4 M_{34}^2}{\omega_o^2 L_4^2 + (R_4 + R_L)^2} \tag{5.20b}$$

It is assumed that capacitance C_3 is chosen so that the reflected reactance $X_{\text{ref}34}$ and inductance L_3 resonate with C_3 at angular frequency ω_o. In this circumstance, the reflected reactance from L_3 to L_2 is zero, as indicated by Eq. (5.14b) above, and the resistance $R_{\text{ref}23}$ reflected into L_2 from L_3 is:

$$R_{\text{ref}23}(\omega_o) = \frac{\omega_o^2 M_{23}^2}{(R_3 + R_{\text{ref}34})^2} = \frac{\omega_o^2 M_{23}^2 \left[\omega_o^2 L_4^2 + (R_4 + R_L)^2\right]}{R_3\left[\omega_o^2 L_4^2 + (R_4 + R_L)^2\right] + \omega_o^2 (R_4 + R_L) M_{34}^2} \tag{5.21}$$

No reactance is coupled from L_2 into L_1 if C_2 and L_2 are also resonant at ω_o; thus the reflected reactance X_{ref} of Fig. 5.8 will be zero. The resistance coupled into L_1 from L_2 is:

$$R_{\text{ref}12}(\omega_o) = \frac{\omega_o^2 M_{12}^2}{(R_2 + R_{\text{ref}23})^2} = \frac{\omega_o^2 M_{12}^2 \left\{ R_3 \left[\omega_o^2 L_4^2 + (R_4 + R_L)^2\right] + \omega_o^2 M_{34}^2 (R_4 + R_L) \right\}}{(R_2 R_3 + \omega_o^2 M_{23}^2)\left[\omega_o^2 L_4^2 + (R_4 + R_L)^2\right] + R_2 \omega_o^2 M_{34}^2 (R_4 + R_L)} \tag{5.22}$$

Assuming v_s is an *rms* quantity, the *rms* magnitude of the current i_1 is:

$$|i_1| = \frac{v_s}{\sqrt{(R_s + R_1 + R_{\text{ref}12})^2 + \left(\omega_o L_1 - \frac{1}{\omega_o C_1}\right)^2}} \tag{5.23}$$

Total power delivered by the sinusoidal voltage source P_{total} is:

$$P_{\text{total}} = \frac{v_s^{\,2}\left(R_s + R_1 + R_{\text{ref}12}\right)}{\left(R_s + R_1 + R_{\text{ref}12}\right)^2 + \left(\omega_o L_1 - \dfrac{1}{\omega_o C_1}\right)^2} \tag{5.24}$$

The efficiency η is:

$$\eta = \frac{R_L}{R_4 + R_L} \times \frac{R_{\text{ref}34}}{R_3 + R_{\text{ref}34}} \times \frac{R_{\text{ref}23}}{R_2 + R_{\text{ref}23}} \times \frac{R_{\text{ref}12}}{R_S + R_1 + R_{\text{ref}12}} \tag{5.25}$$

The reactance X_{ref} reflected into L_1 in Figure 5.8 will be zero if L_2 and C_2 are resonant at ω_o and if the value of C_3 has been chosen so that L_3, reflected reactance $X_{\text{ref}34}$, and C_3 are also resonant at ω_o.

The currents i_2 and i_3 may be calculated by appropriate substitution into Eq. (5.16):

$$i_2 = \frac{-j\omega_o M_{12}}{R_2 + R_{\text{ref}23}} \cdot i_1 \tag{5.26a}$$

$$i_3 = \frac{-j\omega_o M_{23}}{R_3 + R_{\text{ref}34}} \cdot i_2 = \frac{-\omega_o^{\,2} M_{12} M_{23}}{\left(R_2 + R_{\text{ref}23}\right)\left(R_3 + R_{\text{ref}34}\right)} \cdot i_1 \tag{5.26b}$$

Current i_4 may be computed by substitution into Eq. (5.19):

$$i_4 = \frac{-j\omega_o M_{34}}{R_4 + R_L + j\omega L_4} i_3 = \frac{-\omega_o^{\,2} M_{34} M_{23}}{\left(R_4 + R_L + j\omega L_4\right)\left(R_3 + R_{\text{ref}34}\right)} \cdot i_2 \tag{5.27a}$$

$$i_4 = \frac{j\omega_o^{\,3} M_{34} M_{23} M_{12}}{\left(R_4 + R_L + j\omega L_4\right)\left(R_3 + R_{\text{ref}34}\right)\left(R_2 + R_{\text{ref}23}\right)} \cdot i_1 \tag{5.27b}$$

The question may be posed about the effects of the mutual couplings M_{13}, M_{14}, M_{24} that have been ignored in the derivation above. The effect on the effective

inductance of L_1 is of particular interest. If self-inductance L_1 and mutual inductance M_{13} are considered, the voltage v_1 is given by:

$$v_1 = j\omega_o L_1 i_1 + j\omega_o M_{13} i_3 = j\omega_o \left[L_1 - \frac{\omega_o^2 M_{12} M_{23} M_{13}}{(R_2 + R_{ref23})(R_3 + R_{ref34})} \right] \cdot i_1 = j\omega_o L_1' \qquad (5.28)$$

in which i_3 has been expressed in terms of i_1 by means of Eq. (5.26b), transforming inductance L_1 into an effective inductance L_1'.

The effect of M_{13} is to reflect a capacitance C_{ref13} into L_1:

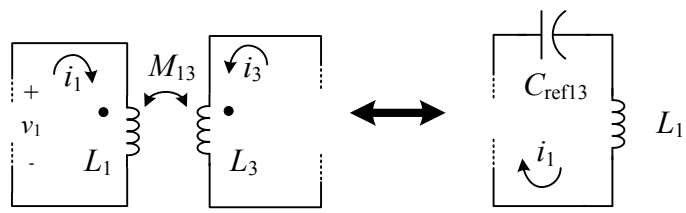

Figure 5.9: Reflection of a capacitive reactance into L_1 due to mutual inductance M_{13} and inductor current i_3

The reflected capacitance may be computed as:

$$C_{ref13} = \frac{(R_2 + R_{ref23})(R_3 + R_{ref34})}{\omega_o^4 M_{12} M_{23} M_{13}} \qquad (5.29)$$

Equations (5.28) and (5.29) raise the possibility that under certain conditions the inductance of L_1 could disappear or become negative (which would mean that the impedance of L_1 at ω_o would become capacitive). Mutual inductances M_{14} and M_{24} will reflect both resistive and reactive components from L_4 into L_1 and L_2, respectively.

5.5 Application of reflected impedances to the design of a four-coil WPT system:

In a four-coil WPT system with a given load resistance R_L and a load power P_L, the load may be transformed into a resistance reflected into L_1 to which power may be delivered appropriate to the *rms* value of the sinusoidal voltage source driving the WPT

system. The reflected resistance must be such that the *rms* sinusoidal voltage source can deliver the expected power.

From Eq. (5.25), it is seen that high efficiency requires that reflected resistances R_{ref34}, R_{ref23}, and R_{ref12} be much greater than the ESRs of the circuits into which they are reflected. The maximal power delivery to the system is limited by the *rms* voltage of the driving source and by resistance reflected into L_1; the reflected resistance R_{ref12} must be commensurate with the expected power transfer and the *rms* voltage of the driving source.

Other considerations relate to the mutual inductance M_{13}. When the WPT system is operating at resonance, the mutual inductance M_{13} is responsible for reflecting capacitive reactance into L_1. The reflected capacitance, given by Eq. (5.29), is seen to be inversely proportional to M_{13}; the reactance of this reflected capacitance is thus proportional to M_{13}. Reduction of M_{13} while maintaining M_{12} should be a major consideration in the physical placement of the inductors.

An additional consideration is raised in the sizing of L_1 when square-wave excitation is used instead of sinusoidal excitation. With sinusoidal excitation, the value of L_1 is in principle immaterial as long as it is sufficient to produce a large-enough value of M_{12}. However, the use of square-wave excitation places an additional constraint on L_1. Currents at harmonic frequencies produce losses in R_1, the ESR of the L_1-C_1 circuit, and in R_S, the output resistance of the driving voltage source. These currents are limited principally by the reactance of L_1; larger values of L_1 reduce these harmonic currents' amplitudes. It is thus preferable to make L_1 large and to achieve the design value of M_{12} by loose coupling of L_1 to L_2. Capacitor C_1 is chosen such that its reactance largely (although not completely) cancels the reactance of L_1at the fundamental frequency of the square wave.

A spreadsheet calculator for design of WPT networks is shown in Figure 5.10. The calculator employs the method of reflected impedances described previously. The spreadsheet calculates resistance $R_{ref34}$and reactance X_{ref34}reflected into L_3 from L_4. It then calculates the resistance R_{ref23} reflected from L_3 into L_2.Assuming that capacitor C_3 resonates with L_3 at the operating frequency, the reactance reflected from L_3 into L_2 is zero. The resistance reflected from L_2 into L_1 is computed; if C_2 resonates with L_2, at the

operating frequency, the reactance reflected from L_2 into L_1 is zero. A capacitive reactance reflected from L_3 into L_1 is included. The input current is computed from the *rms* value of the voltage source V_s and the input impedance of the WPT network. Input power and output power are then computed, as well as efficiency.

			Computation of reflected impedances in a resonant four-coil wireless power-transfer system		
			David M. Beams, PhD, PE		
			25-Mar-12		
Operating frequency f:	1.00E+05	Hz	Resistance reflected from L4 into L3 (Rref34):	3.113	Ω
ω:	6.28E+05	rad/s	Reactance reflected from L4 into L3 (Xref34):	-3.914	Ω
Input inductor L1:	33.640	µH	Total resistance of L3 (reflected resistance plus L3 ESR):	3.193	Ω
Inductor L2:	35.240	µH			
Inductor L3:	32.340	µH	Effective inductance of L3:	26.110	µH
Output inductor L4:	11.190	µH	Resonating capacitor C3:	97.01	nF
L1-L2 flux-coupling k12:	0.2390				
L2-L3 flux-coupling k23:	0.1072		Resistance reflected from L3 into L2 (Rref23):	1.619	Ω
L3-L4 flux coupling k34:	0.5608		Total resistance of L2 (reflected resistance plus L2 ESR):	1.705	Ω
Calculated mutual inductance M12:	8.229	µH			
Calculated mutual inductance M23:	3.619	µH	Resonating capacitor C2:	71.88	nF
Calculated mutual inductance M34:	10.668	µH			
ESR of L1:	0.08	Ω	Resistance reflected from L2 into L1 (Rref12):	15.678	Ω
ESR of C1:	0	Ω	Total resistance of L1 (reflected resistance plus L1 ESR):	15.758	Ω
Total ESR (R1) of L1/C1:	0.08	Ω			
ESR of L2:	0.086	Ω	Reactance reflected from L3 into L1 (Xref13):	0.000	Ω
ESR of C2:	0	Ω			
Total ESR (R2) of L2/C2:	0.086	Ω	Impedance of L1:	26.316	Ω
ESR of L3:	0.08	Ω	Phase of impedance of L1:	53.4	deg
ESR of C3:	0	Ω			
Total ESR (R3) of L3/C3:	0.08	Ω	I1(mag):	0.128	Arms
Total ESR (R4) of L4:	0.042	Ω	I1(phase):	-0.577	rad
Load resistance RL:	5.55	Ω	I1(phase):	-33.1	deg
Voltage source resistance RS:	0.5	Ω	Input power:	0.3	W
Voltage source rms value Vs:	2.49	Vrms	Load power:	0.2	W
Input capacitance C1:	150.9	nF	Efficiency:	88.6%	
L1-L3 flux-coupling k13:	0.0000				

Figure 5.10: WPT design worksheet based on reflected impedances

The proposed design methodology using impedance transformation for WPT systems is as follows:

1. Compute the resistance R_{ref12} to be reflected into L_1 from L_2 given the operating frequency, the *rms* value of the excitation voltage, and the power to be delivered to the load. (For square-wave excitation, this would be the *rms* value of the fundamental component of the square wave, which is $0.4502 \times V_{pp}$, where V_{pp} is the peak-to-peak voltage of the square wave). The entire *rms* voltage will not be developed across this reflected resistance since it is desirable to have the WPT

network present a load having inductive reactance as well as resistance to the driving-point source.

2. Determine values of inductors L_1–L_4 and flux-coupling coefficients k_{12}, k_{23}, and k_{34} to produce the transformation from load resistance R_L into R_{ref12}. The spreadsheet shown in Fig. 9 may be used for this purpose. Estimation of ESRs is required for an estimate of efficiency.
3. Determine a value of capacitor C_1 that makes the input impedance of the WPT network somewhat inductive at the operating frequency. (It is suggested that the phase of current I_1 lag the excitation voltage by 30–50° at the excitation frequency).
4. The inductors may be designed for the specified self-inductances using the Matlab coil-creation software that has been developed by the University of Texas at Tyler for this project.
5. Locations of the coils with respect to each other to produce the design flux-coupling coefficients may be investigated with the mutual-inductance calculation software developed by the University of Texas at Tyler. This software may also be used to calculate the incidental coupling coefficients k_{13}, k_{14}, and k_{24}.
6. The Matlab WPT simulation may be used to predict system performance once values of inductances, flux-coupling coefficients, resistor values, and capacitor values have been entered.
7. For square-wave drive, the network should be simulated at odd harmonics of the excitation frequency with appropriate *rms* values to determine the losses due to harmonic currents. If these losses are excessive, L_1 may be increased and k_{12} reduced (to maintain the design value of M_{12}); the value of C_1 will have to be reduced to increase its reactance to maintain the target phase angle of I_1.

5.6 Validation of the design methodology using impedance transformation

Four spiral-wound coils were arranged in parallel and co-axial manner as shown in Figure 5.11, and their respective self-inductances were calculated by the methods described in Chapter Four and compared to measured values determined at 100 kHz using the "L_s" measurement mode of the 4362 LCR Bridge.

Figure 5.11 shows the arrangements of coils used in validation process of the design method of four-coil WPT in which the distances between coils L_1- L_2 and L_3–L_4 are constant (48.3mm and 15.2mm),while the distance between L_2 and L_3 (designated as D_{23}) can be varied.

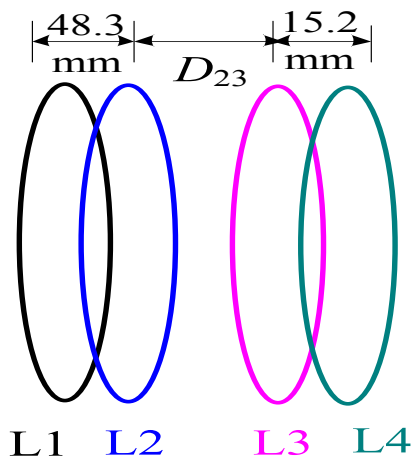

Figure 5.11: Physical arrangement of single-layer spiral coils used in validation experiments

Three different sets of experiments were conducted by varying the distance D_{23} between the coils L_2–L_3 in the Figure 5.11. General experimental validations is described in detail in the following section (5.6.1); Section 5.6.2 compares results from both calculated and measured values for all three experiments with varying values of D_{23}.

The physical arrangement of the coils used in validation of WPT system design is shown in Figure 5.12. Coils L_1-L_3 are attached to their respective capacitors C_1-C_3 and coil L_4 terminated with load R_L. The load resistance was composed of a number of 50Ω non-inductive thick-film resistors.

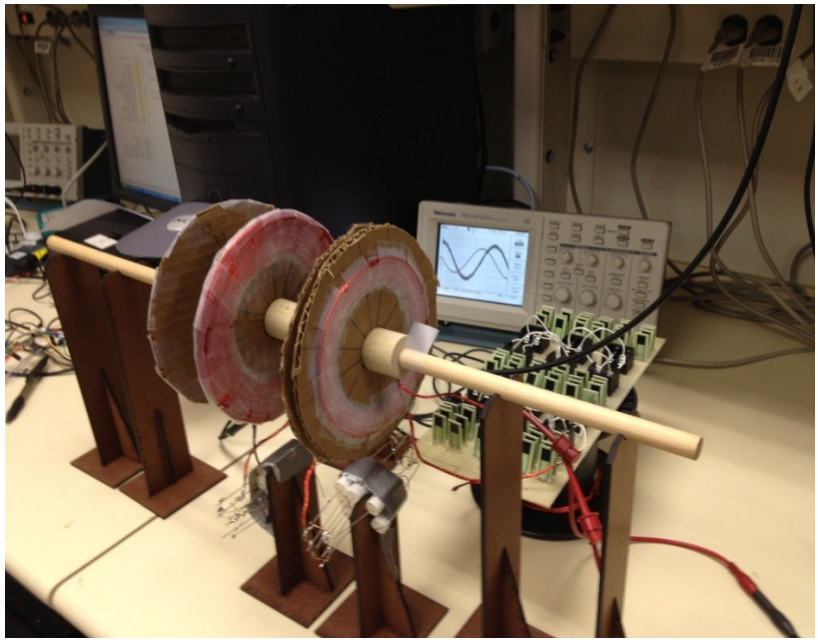

Figure 5.12 Experimental apparatus, showing physical arrangement of coils, resonating capacitors, and load resistance

5.6.1 Experimental method of design validation

After entering all the input parameters into the design spreadsheet (Figure 5.10), it calculates all the above mentioned parameters involved in the system and designed work sheet is verified by experiments by building the practical model of the four-coil WPT system.

Validation began by calculating the reflected impedance looking into L_3 with coil L_4 terminated with a non-inductive load resistance R_L. This is represented by the network shown in Figure 5.13 with this connection; measured resistance R_{eff3} and effective inductance L_{eff3} were measured at 100 kHz using the "L_s" measurement mode of the 4362 LCR Bridge.

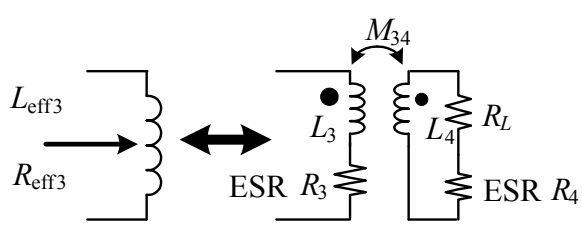

Figure 5.13: Measured resistance and effective inductance of L_3 (including resistance and reactance reflected into L_3 from L_4)

In the second step, coil L_3 was paralleled with capacitor C_3 whose value was calculated to resonate with L_{eff3} at 100 kHz. . Coil L_4 is terminated with load R_L as before. This network is shown in Figure 5.14.The impedance looking into L_2 was measured as a series connection of an inductance L_{eff2} and a resistance R_{eff2}.

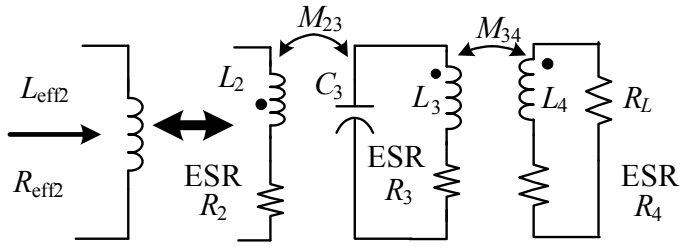

Figure 5.14: Measured resistance and inductance looking into L_2

With this termination, R_{eff2} andL_{eff2} were measured at 100 kHz using the "L_s" measurement mode of the Agilent 4362 LCR Bridge.

A similar process is carried out by connecting L_2 with the capacitor C_2 whose value was calculated to resonate with L_{eff2} at 100 kHz. Coils L_3 and L_4 were terminated as before. The network now appears as in Figure 5.15. The effective inductance L_{eff1} and R_{ref1} at the terminals of L_1 were measured.

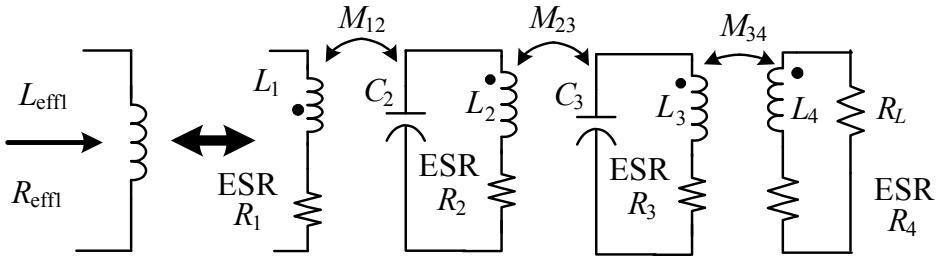

Figure 5.15: Measured resistance and inductance looking into L_1

The circuit of Figure 5.15 was modified by connecting C_1 to one of the terminals of coil L_1. A small series resistance R_s (to serve as a current-sense resistor) was connected to the other terminal. An HP 33120A waveform generator set to produce a 100 kHz sinusoid was connected to the input terminals of the WPT network, as shown in Figure 5.16. Input voltage v_{in} was measured, and input current (magnitude and phase) was determined from the voltage across the 0.49Ω current-sense resistor. The magnitude and phase of output voltage across the load R_L were also measured.

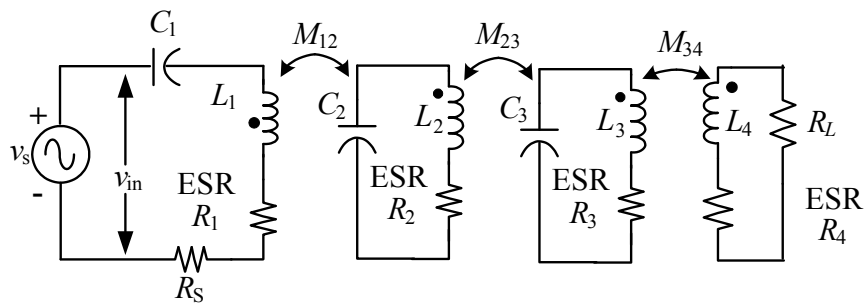

Figure 5.16: Connection of the WPT network to a sinusoidal signal source

5.6.2 Summary of experimental results

The following section summarizes results of the experimental procedure in Section 5.6.1 for three different values of D_{23} (63.6mm, 78mm, and 102mm). Experimental results obtained from all the three tests are compared with calculated values and are tabulated (Tables 5.3-5.7) below for ease of comparison between each individual experiment.

Self-inductances used in all three experiments are fixed; similarly, the mutual inductances between the coils L_1 and L_2 (M_{12}) and L_3 and L_4 (M_{34}) are fixed. The measured values of these fixed inductances are tabulated in Table 5.1. Included also are the measured ESRs of the coils.

Table 5.1: Fixed self- and mutual inductances in design-validation experiments

L_1, μH	33.77	ESR, Ω	0.080
L_2, μH	35.48	ESR, Ω	0.086
L_3, μH	32.37	ESR, Ω	0.080
L_4, μH	11.32	ESR, Ω	0.042
M_{12}, μH	8.29		
M_{34}, μH	10.22		

Mutual inductances between the coils L_1– L_3 (M_{13}), L_1 – L_4 (M_{14}), L_2–L_3 (M_{23}) and L_2–L_4 (M_{24}) are tabulated below (Table 5.2) as a function of coil separation D_{23}.

Table 5.2: Variable mutual inductances vs. source-to-load spacing D_{23}

	D_{23} = 63.5 mm	D_{23} = 78.0 mm	D_{23} = 102 mm
M_{13}, μH	2.07	1.40	0.92
M_{14}, μH	0.76	0.53	0.42
M_{23}, μH	5.46	3.62	2.20
M_{24}, μH	2.01	1.36	0.85

Resistor R_L (measured value 5.55Ω) was added to the terminals of L_4 to produce the network of Figure 5.13. Table 5.3 below gives results for the measured inductance and reactance at the terminals of L_3 and compares them with expectations from the design spreadsheet. The value of reflected resistance R_{ref34} cannot be measured directly; the calculated total resistance at the terminals of L_3 is the sum of the calculated reflected resistance R_{ref34} and the measured ESR of L_3. Similarly reflected reactance X_{ref34} cannot be measured; the expected inductance L_{eff3} was computed from the expected reflected reactance X_{ref34} and the measured self-inductance of L_3.

Table 5.3: Reflected resistance and reactance from coil 4 into coil 3, and inductance and resistance measured at the terminals of L_3 for the network of Figure 5.13. R_{eff3}, the calculated total resistance at the terminals of L_3, is the sum of the calculated reflected resistance R_{ref34} and the measured ESR of L_3.

	Calculated	Measured
X_{ref34}, Ω	-3.58	–
L_{eff3}, μH	26.67	26.16
R_{ref34}, Ω	2.82	–
R_{eff3}, Ω	2.90	2.95

Capacitor C_3 (measured value 97.40nF) was added to the terminals of L_3 to produce the network of Figure 5.13. Table 5.4 below gives results for the measured inductance and reactance at the terminals of L_2 for this network and compares them with expectations from the design spreadsheet. The value of reflected resistance R_{ref23} cannot be measured directly; the calculated total resistance at the terminals of L_2 is the sum of the calculated reflected resistance R_{ref23} and the measured ESR of L_2. Inductance L_{eff2} was

measured at the terminals of L_2; no calculation of expected effective value of L_2 was made, however, since no reactance is reflected into L_2 if L_3/C_3 are resonant at the operating frequency.

Table 5.4: Reflected resistance from coil 3 into coil 2, total resistance at the terminals of L_2 (R_{eff2}), and measured inductance of L_2 (L_{eff2}) vs source-to-load spacing D_{23} for a network similar to that of Figure 5.14. R_{eff2} is the sum of the calculated reflected resistance R_{ref23} and the measured ESR of L_2.

	D_{23} = 63.5 mm		D_{23} = 78.0 mm		D_{23} = 102 mm	
	Calculated	Measured	Calculated	Measured	Calculated	Measured
R_{ref23}, Ω	4.06	–	1.79	–	0.64	–
R_{eff2}, Ω	4.15	2.40	1.88	1.08	0.73	0.46
$Leff_2$, μH	–	32.96	–	34.38	–	34.92

Capacitor C_2 (measured value 71.75nF) was added to the terminals of L_2 to produce the network of Figure 5.14. Table 5.5 below gives results for the measured inductance and reactance at the terminals of L_1 and compares them with expectations from the design spreadsheet. The value of reflected resistance R_{ref12} cannot be measured directly; the calculated total resistance at the terminals of $L_1$is the sum of the calculated reflected resistance $R_{ref12}$and the measured ESR of L_1. Inductance L_{eff1} was measured, but no calculation of expected value of L_1 was made since no reactance is reflected into L_1 if L_2/C_2 are resonant at the operating frequency.

Table 5.5: Reflected resistance from coil 2 into coil 1, total resistance at the terminals of L_1 (R_{eff1}), and measured inductance of L_1 (L_{eff1}) vs. source-to-load spacing D_{23} for a network similar to that of Figure 5.15. R_{eff1} is the sum of the calculated reflected resistance R_{ref12} and the measured ESR of L_1.

	D_{23} = 63.5 mm		D_{23} = 78.0 mm		D_{23} = 102 mm	
	Calculated	Measured	Calculated	Measured	Calculated	Measured
R_{ref12}, Ω	6.52	–	14.4	–	36.2	–
R_{eff1}, Ω	6.60	8.26	14.5	19.1	36.3	45.4
L_{eff1}, μH	–	35.87	–	44.73	–	61.19

Table 5.6 below summarizes the measured input voltages V_S and calculated and measured input currents I_1 for the WPT network driven by a 100.00 kHz sinusoidal voltage.

Table 5.6: Input voltage V_S and magnitude and phase of input current I_1 vs. source-to-load spacing D_{23}.

	D_{23} = 63.5 mm		D_{23} = 78.0 mm		D_{23} = 102 mm	
	Calculated	Measured	Calculated	Measured	Calculated	Measured
V_S, V rms	1.78		2.50		3.88	
$\|I_1\|$, A rms	0.139	0.125	0.136	0.116	0.101	0.074
phase, deg	–56.3	–53.0	–35.5	–52.0	–16.2	–38.0
V_{RL}, V rms	-	0.75	-	0.927	-	0.96

The efficiency was calculated as the ratio of output power to input power. Calculated and measured values are summarized in Table 5.7 below.

Table 5.7: Efficiency of power transfer of the WPT network

	D_{23} = 63.5 mm		D_{23} = 78.0 mm		D_{23} = 102 mm	
	Calculated	Measured	Calculated	Measured	Calculated	Measured
η, %	86.8	77.2	88.5	87.0	84.1	76.0

5.6.3 Discussion

Measured reflected resistance into L_2 is considerably smaller when compared to calculated value; this is shown in the values of R_{eff2} in Table 5.4. This occurs because the proposed design model ignores the effect of M_{24}. Figure 5.17 shows a portion of the WPT network consisting of L_2, L_3, and L_4 (and their associated ESRs); load resistor R_L; and capacitor C_3. Figure 5.17 includes mutual inductance M_{24}, which was omitted from the design worksheet.

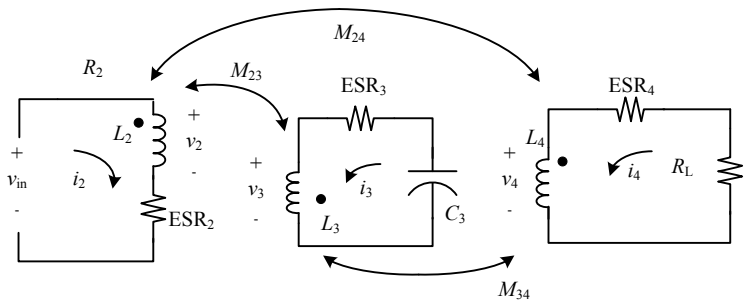

Figure 5.17: Network including M_{24}

Following are equations that describe above network shown in Figure 5.17:

$$
\begin{aligned}
& j\omega L_2 i_2 + j\omega M_{23} i_3 + j\omega M_{24} i_4 - v_2 = 0 \\
& j\omega L_3 i_3 + j\omega M_{23} i_2 + j\omega M_{34} i_4 - v_3 = 0 \\
& j\omega L_4 i_4 + j\omega M_{34} i_3 + j\omega M_{24} i_2 - v_4 = 0 \\
& (ESR_3 + \frac{1}{j\omega C_3}) i_3 + v_3 = 0 \\
& (R_L + ESR_3) i_4 + v_4 = 0 \\
& i_2 ESR_2 + v_2 = v_{in}
\end{aligned}
\tag{5.30a–f}
$$

Eqs. (5.30a–f) may be expressed in matrix form as:

$$
\begin{bmatrix}
j\omega L_2 & j\omega M_{23} & j\omega M_{24} & -1 & 0 & 0 \\
j\omega M_{23} & j\omega L_3 & j\omega M_{34} & 0 & -1 & 0 \\
j\omega M_{24} & j\omega M_{34} & j\omega L_4 & 0 & 0 & -1 \\
0 & ESR_3 + 1/j\omega C_3 & 0 & 0 & 1 & 0 \\
0 & 0 & R_L + ESR_4 & 0 & 0 & 1 \\
0 & ESR_2 & 0 & 1 & 0 & 0
\end{bmatrix}
\times
\begin{bmatrix} i_2 \\ i_3 \\ i_4 \\ v_2 \\ v_3 \\ v_4 \end{bmatrix}
\equiv
\begin{bmatrix} 0 \\ 0 \\ 0 \\ 0 \\ 0 \\ v_{in} \end{bmatrix}
\tag{5.31}
$$

The impedance looking into coil L_2 is v_{in}/i_2.A solution to Eq. (5.31) was computed with parametric values from the case of D_{23} = 78mm, and the input impedance was computed as 0.9665 + j 21.6 Ω. The resistive component of this value includes both the reflected resistance and the ESR of L_2; it is thus the expected value of the resistive component at the terminals of L_2. The corresponding measured value from Table 5.4 is 1.08Ω, which is considerably closer to 0.9665Ω than the expected value (1.88Ω). The

discrepancies between calculated and measured values of resistance at the terminals of L_2 in Table 5.4 appear to be due to the effects of M_{24}, which were ignored in the design worksheet.

The measured inductances of L_1 reported in Table 5.5 are greater than the actual measured self-inductance of L_1. This observation may be explained if the resonant frequency of L_2/C_2 were slightly higher than the operating frequency; it is noted in Figure 5.6 that the apparent inductance of the primary winding of a transformer with a resonant secondary exceeds the primary self-inductance at frequencies just below resonance of the secondary. This effect cannot be attributed to mutual inductance M_{13} because as shown in Eq. (5.29), the reactance reflected into L_1 from L_3 will be capacitive. (The design spreadsheet allows the designer to include a value for flux-coupling coefficient k_{13}. A value greater than zero causes the value of L_1 to be corrected by the calculated reflected capacitance. However, flux-coupling coefficient k_{13} was set to zero for the work presented above).

5.7 Summary

The method of designing WPT systems using reflected impedances in loosely-coupled coils is validated with both experimental and theoretical data. However, the WPT system design method neglects the mutual inductance M_{24} which reduces the resistance reflected into L_2, which limits the maximal efficiency of the WPT network. This finding thus calls into question the design model. It has been shown that including M_{24} in the design corrects the discrepancies between calculated and measured values of resistance at the terminals of L_2. The large deviation of effective value of L_1 from expectations shows the sensitivity of the WPT system. Giving consideration to these findings, however, the direct design process outlined above does appear to be useful in first-pass design which may then be refined or improved by analysis with the complete model.

Chapter Six
Conclusions and future work

6.1 Conclusions

The primary data gathered from the performed experiments is useful in shaping the future of the wireless power transfer, as it progresses toward high power and efficiency goals. In this thesis developed numerical tools used for designing and analyzing four-coil wireless power transfer are successfully demonstrated with experiments.

Proposed Model of four-coil WPT network described in Chapter Three of the thesis was incorporated into Matlab simulator tool and validated with experimental work.

Method of magnetic vector potential for computation of self- and mutual inductances was incorporated into Matlab simulator tools and validated. Matlab based numerical tools used for calculating the self- and mutual inductances of the coil are developed by using magnetic vector potential method which acts as a substitute for Finite Element Analysis (FEA) where the user needs to have prior knowledge of the software.

Design methodology using reflected impedances in loosely-coupled inductors for a four-coil WPT network was presented and found to be useful, although the simple model's predictions are significantly affected by mutual couplings that the model ignores. The efficiencies reached by the designed model described in Chapter Five of the thesis were over 76% with an air gap distance of about 102mm.

6.2 Future work

The immediate extension of this thesis could be validating the designed four-coil method under non co-axial and non-parallel geometries with nonlinear (instead of resistive) loads and by driving the designed system with non-square rectangular inputs for harmonic suppression and compare it with the designed numerical tools.

Study of the effects of component tolerances, multiple receivers with agile frequency selection and high-permeability materials to shape magnetic fields on the performance of the designed system.

References

[1] Zhong, W.X.; Liu, X.; Hui, S.Y.R. "Analysis on a single-layer winding array structure for contactless battery charging systems with free-positioning and localized charging features." *Proceedings of the 2010 IEEE Energy Conversion Congress and Exposition (ECCE),* pp. 658-665, 2010.

[2] Meyer, P.; Germano, P.; Markovic, M.; Perriard, Y."Design of a Contactless Energy-Transfer System for Desktop Peripherals," *IEEE Transactions on Industry Applications,* vol.47, no.4, pp.1643-1651, July-Aug. 2011.

[3] Hori, Y. "Application of Electric Motor, Supercapacitor, and Wireless Power Transfer to enhance operation of future vehicles*," Proceedings of the 2010 IEEE International Symposium on Industrial Electronics (ISIE 2010),* pp. 3633-3635, 2010.

[4] Guozheng Yan; Dongdong Ye; Peng Zan; Kundong Wang; Guanying Ma. "Micro-Robot for Endoscope Based on Wireless Power Transfer." *Proceedings of the International Conference on Mechatronics and Automation (ICMA 2007),* pp. 3577-3581, 2007.

[5] Seung-Hwan Lee; Lorenz, R.D. "Development and validation of model for 95% efficiency, 220 W wireless power transfer over a 30cm air-gap," *Energy Conversion Congress and Exposition (ECCE), 2010 IEEE,* pp.885-892, Sept.2010.

[6] N. Tesla, *"Apparatus for Transmission of Electrical Energy,"* U.S. Patent 649,621, May 15, 1900.

[7] http://www.tfcbooks.com/articles/monument.htm , accessed February 26, 2012.

[8] Terman, F.E.; "A brief history of electrical engineering education," *Proceedings of the IEEE,* vol.64, no.9, pp. 1399- 1407, Sept. 1976 .

[9] Brown, W.; Mims, J.; Heenan, N.; “An experimental microwave-powered helicopter," *IRE International Convention Record,* pp. 225- 235, Mar 1965.

[10] http://www.witricity.com/, accessed February 28, 2012.

[11] http://www.iportmusic.com/products/launch, accessed March 3, 2012.

[12] http://www.wirelesspowerplanet.com/news/samsung-wireless-charging-hub-for-3d-glasses/ , accessed March 6, 2012.

[13] Cannon, B.L.; Hoburg, J.F.; Stancil, D.D.; Goldstein, S.C.; , "Magnetic Resonant Coupling As a Potential Means for Wireless Power Transfer to Multiple Small Receivers," *IEEE Transactions on Power Electronics ,* vol.24, no.7, pp.1819-1825, July 2009.

[14] Shen, F. Z.; Cui, W. Z.; Ma, W.; Huangfu, J. T.; Ran, L. X.; , "Circuit analysis of wireless power transfer by ‘coupled magnetic resonance’," *IET International Communication Conference on Wireless Mobile and Computing (CCWMC 2009)*, pp.602-605, Dec. 2009.

[15] Zhen Ning Low; Chinga, R.A.; Tseng, R.; Jenshan Lin; "Design and Test of a High-Power High-Efficiency Loosely Coupled Planar Wireless Power Transfer System," *IEEE Transactions on Industrial Electronics,,* vol.56, no.5, pp.1801-1812, May 2009.

[16] J. Choi and C. Seo, “High-Efficiency Wireless Energy Transmission Using Magnetic Resonance Based on Negative Refractive Index Metamaterial,” *Progress In Electromagnetics Research,* vol. 106, pp. 33-47, 2010.

[17] Aristeidis Karalis, J.D. Joannopoulos, and Marin Soljačić, “Efficient wireless non-radiative mid-range energy transfer,” *Annals of Physics,* vol. 323, no. 1, pp. 34-48, Jan 2008.

[18] Ping Si; Hu, A.P.; Malpas, S.; Budgett, D. "A Frequency Control Method for Regulating Wireless Power to Implantable Devices," *IEEE Transactions on Biomedical Circuits and Systems*, vol.2, no.1, pp.22-29, March 2008.

[19] Teck Chuan Beh, Takehiro Imura, Masaki Kato, Yoichi Hori, "Basic Study of Improving Efficiency of Wireless Power Transfer via Magnetic Resonance Coupling Based on Impedance Matching" *International Symposium on Industrial Electronics,* pp. 2011-2016, 2010.

[20] Chih-Jung Chen; Tah-Hsiung Chu; Chih-Lung Lin; Zeui-Chown Jou; , "A Study of Loosely Coupled Coils for Wireless Power Transfer,"*IEEE Transactions on Circuits and Systems II: Express Briefs,* vol.57, no.7, pp.536-540, July 2010.

[21] Kurs, A. Karalis, R. Moffatt, J. D. Joannopoulos, P. Fisher, and M. Soljacic, "Wireless Energy Transfer via Strongly Coupled Magnetic Resonances," *Science* 317, pp. 83-86, 2010.

[22] Su, Y.P.; Xun Liu; Hui, S.Y.R.; "Mutual inductance calculation of movable planar coils on parallel surfaces," *IEEE 2008 Power Electronics Specialists Conference* (*PESC 2008*), pp.3475-3481, 15-19 June 2008.

[23] Z. Low, J. Casanova and J. Lin, "A Loosely Coupled Planar Wireless Power Transfer System Supporting Multiple Receivers," *IEEE Transactions on Industrial Electronics*, vol.56, no.8, pp. 3060-3068, August 2009.

[24] Xin W H, Yan G Z and Wang W X, "Study of a wireless power transmission system for an active capsule endoscope," *Int. J Med Robot*, pp. 113-122, March 2010.

[25] Imura T, Uchida T, Hori Y, "Flexibility of contactless power transfer using magnetic resonance coupling to air gap and misalignment for EV," *World Electric Vehicle Journal* Vol. 3, pp. 1-10, 2009.